



Reverberation Mapping of Luminous Quasars at High z

Paulina Lira¹, Shai Kaspi², Hagai Netzer³ , Ismael Botti⁴, Nidia Morrell⁵ , Julián Mejía-Restrepo¹ , Paula Sánchez-Sáez¹ ,
Jorge Martínez-Palomera¹ , and Paula López¹

¹ Departamento de Astronomía, Universidad de Chile, Casilla 36D, Santiago, Chile

² Wise Observatory, School of Physics and Astronomy, Tel Aviv University, Tel Aviv 69978, Israel

³ School of Physics and Astronomy, Tel Aviv University, Tel Aviv 69978, Israel

⁴ Facultad de Ingeniería, Universidad del Desarrollo, Av. Plaza 680, Las Condes, Santiago, Chile

⁵ Las Campanas Observatory, Carnegie Observatories, Casilla 601, La Serena, Chile

Received 2017 July 7; revised 2018 July 27; accepted 2018 July 28; published 2018 September 20

Abstract

We present reverberation mapping (RM) results for 17 high-redshift, high-luminosity quasars with good-quality R -band and emission-line light curves. We are able to measure statistically significant lags for Ly α (11 objects), Si IV (5 objects), C IV (11 objects), and C III] (2 objects). Using our results and previous lag determinations taken from the literature, we present an updated C IV radius–luminosity relation and provide for the first time radius–luminosity relations for Ly α , Si IV, and C III]. While in all cases the slopes of the correlations are statistically significant, the zero points are poorly constrained because of the lack of data at the low-luminosity end. We find that the emissivity-weighted distances from the central source of the Ly α , Si IV, and C III] line-emitting regions are all similar, which corresponds to about half that of the H β region. We also find that 3/17 of our sources show an unexpected behavior in some emission lines, two in the Ly α light curve and one in the Si IV light curve, in that they do not seem to follow the variability of the UV continuum. Finally, we compute RM black hole (BH) masses for those quasars with highly significant lag measurements and compare them with C IV single-epoch (SE) mass determinations. We find that the RM-based BH mass determinations seem smaller than those found using SE calibrations.

Key words: quasars: general – quasars: supermassive black holes

Supporting material: figure set, machine-readable table

1. Introduction

These days it is widely accepted that all massive galaxies harbor a massive black hole (BH) in their centers (Kormendy & Ho 2013). To determine the properties of these BHs is therefore crucial for the understanding of galaxy formation and evolution. The ability to measure BH masses and accretion rates in active galactic nuclei (AGNs) using reverberation mapping (RM) techniques has enabled real physical comparison between active and dormant BHs in the local universe, but BH mass estimates from AGNs become even more crucial at high z since stellar dynamical estimates from the study of normal galaxies are clearly not feasible at redshifts of cosmological interest ($z > 1$).

RM uses the lag between variations in the central ionizing source and the response of the broad-line region (BLR) emission lines to directly measure the BLR size (Blandford & McKee 1982). Assuming a gravitationally bound system and measuring the BLR line widths, it is possible to infer the mass of the central BH. This assumption has proven to be correct for those objects with measurements from several lines: the observed anticorrelation between the line Doppler widths and their distance from the central BH is consistent with virialized motion of the BLR gas in the deep potential of the central BH (Onken & Peterson 2002).

To date RM results cover almost 5 orders of magnitude in luminosity but are still limited to luminosities $\lambda L_{\lambda}(5100 \text{ \AA}) < 10^{46} \text{ erg s}^{-1}$, with the bulk of sources found well below $< 10^{45} \text{ erg s}^{-1}$ (e.g., Kaspi et al. 2000, 2005, 2007; Peterson et al. 2004; Bentz et al. 2006, 2009, 2013). Hence, such results cannot be directly applied to high- z , high-luminosity sources, which contain the most massive BHs, since measuring their

BLR size requires an extrapolation by up to *two orders of magnitude* in luminosity. This hampers the calibration of the so called radius–luminosity relations, which enable the determination of BH masses from a single spectroscopic observation without requiring source monitoring. “Single-epoch (SE)” BH mass determinations are readily obtained from large spectroscopic surveys but require the extrapolation of the radius–luminosity relation when high- z , high-luminosity quasars are studied. It is therefore clear that to have statistically significant results for BH demographics and their mass growth with cosmic time, it is first necessary to determine well-calibrated radius–luminosity relations that are representative of the full span of AGN luminosity.

So far the few attempts to carry out RM of very high luminosity quasars have seldom proved successful (e.g., Welsh et al. 2000; Trevese et al. 2006; Kaspi et al. 2007; Trevese et al. 2014; Saturni et al. 2016). There are mainly two reasons for this: first, most high-luminosity sources show very low amplitude variations ($< 20\%$) on short timescales and require very extended (many years) monitoring to observe significant flux variations and to overcome the $(1 + z)$ time delay. Second, as is usually observed in monitoring campaigns, amplitudes for emission-line light curves are smaller than those of the continuum emission, as the emission-line response is averaged over the very large ($\sim 1 \text{ pc}$) quasar BLR geometry. As monitoring of high- z , high-luminosity quasars often only samples a few, low-amplitude continuum flux variation “events,” the line response can become extremely weak. This requires the ability to measure emission-line fluxes to an accuracy of about a few percent (e.g., Kaspi et al. 2007) and the implementation of tailored observing strategies.

Table 1
Sample Summary

Quasar	z	R.A. Decl. (J2000)	R (mag)	$\lambda_{L\lambda}(1350 \text{ \AA})$ ($10^{46} \text{ erg s}^{-1}$)	$\lambda_{L\lambda}(5100 \text{ \AA})$ ($10^{46} \text{ erg s}^{-1}$)	$P_{843 \text{ MHz}}$ (mJy)	$P_{1.4 \text{ GHz}}$ (mJy)	R_{radio}	$M_{\text{BH}}^{\text{SE}}(\text{C IV})$ ($10^9 M_{\odot}$)
CT1061	3.373	10 48 56 -16 37 09	16.20 ± 0.12	33.88 ± 3.15	10.28 ± 0.12	N/A	<0.5	<1	3.42
CT250	2.407	04 11 45 -42 54 44	17.69 ± 0.14	4.97 ± 0.99	2.88 ± 0.07	<6	N/A	<21	4.65
CT252	1.890	04 18 10 -45 32 17	16.40 ± 0.10	0.00 ± 0.00	3.03 ± 0.06	<6	N/A	<6	1.26
CT286	2.556	10 17 23 -20 46 58	16.89 ± 0.13	11.16 ± 1.83	6.28 ± 0.13	N/A	17.7 ± 0.7	48 ± 10	2.27
CT320	2.956	13 17 44 -31 47 13	17.82 ± 0.11	6.35 ± 0.91	3.86 ± 0.07	<6	<0.5	<2	6.23
CT367	2.601	22 00 36 -35 02 17	17.14 ± 0.14	5.89 ± 1.80	4.66 ± 0.18	<6	<0.5	<1	5.01
CT406	3.183	10 39 09 -23 13 25	17.66 ± 0.13	8.13 ± 0.75	6.18 ± 0.07	N/A	3.0 ± 0.5	8.4 ± 3.4	4.80
CT564	2.659	21 50 15 -44 11 23	17.05 ± 0.12	9.95 ± 1.51	3.65 ± 0.07	<6	N/A	<10	1.99
CT650	2.662	04 55 22 -42 16 17	17.28 ± 0.11	7.59 ± 1.83	4.77 ± 0.14	<6	N/A	<16	1.88
CT803	2.741	00 04 48 -41 57 28	17.02 ± 0.12	10.11 ± 1.20	8.20 ± 0.12	<6	N/A	<5	4.09
CT953	2.535	21 59 54 -40 05 50	17.00 ± 0.11	9.99 ± 1.97	6.12 ± 0.15	<6	N/A	<7	5.98
CT975	2.866	22 38 13 -32 48 24	17.46 ± 0.17	8.78 ± 1.57	4.70 ± 0.11	<6	<0.5	<3	5.35
HB89 0329–385	2.433	03 31 06 -38 24 05	17.54 ± 0.12	5.80 ± 0.93	5.40 ± 0.11	24.3 ± 1.3	29.8 ± 1.0	50 ± 9	6.74
2QZ J002830	2.403	00 28 30 -28 17 06	17.05 ± 0.14	8.98 ± 1.74	3.76 ± 0.09	N/A	<0.5	<1	7.64
2QZ J214355	2.620	21 43 55 -29 51 59	17.17 ± 0.11	9.17 ± 1.02	2.82 ± 0.04	N/A	<0.5	<2	5.63
2QZ J221516	2.706	22 15 16 -29 44 23	16.71 ± 0.14	14.29 ± 1.86	10.18 ± 0.17	N/A	467 ± 14	576 ± 100	1.56
2QZ J224743	2.590	22 47 43 -31 03 07	16.65 ± 0.10	13.00 ± 1.05	4.29 ± 0.04	<6	2.7 ± 0.6	5.9 ± 2.8	15.55

Note. Radio fluxes at 843 MHz and 1.4 GHz were taken from the SUMSS and NVSS catalogs, respectively. N/A implies that the sources were not covered by the footprint of the survey. R_{radio} was obtained using the $P_{1.4 \text{ GHz}}$ measurements, except for unavailable objects (“N/A”), where $P_{843 \text{ MHz}}$ was used instead. $\lambda_{L\lambda}(1350 \text{ \AA})$ measurements were obtained from the spectroscopic data. $\lambda_{L\lambda}(5100 \text{ \AA})$ luminosities were obtained either from 2MASS photometry or by extrapolating our own R -band magnitudes (see text). Uncertainties in $\lambda_{L\lambda}(1350 \text{ \AA})$ and $\lambda_{L\lambda}(5100 \text{ \AA})$ were assumed to correspond to the observed R -band variability. SE BH masses ($M_{\text{BH}}^{\text{SE}}$) have been obtained using the measured C IV FWHM (Mejía-Restrepo et al. 2016).

In this article we present results from a $\gtrsim 10$ yr monitoring of high- z , high-luminosity quasars. In Section 2 we describe the sample selection and data acquisition and treatment. Section 3 deals with time series analysis, while Section 4 presents the specifics on the cross-correlation analysis. Section 5 presents the results for the radius–luminosity relations. Finally, Sections 6 and 7 discuss and summarize the findings. A concordance cosmology with $\Omega_m = 0.3$ and $\Omega_{\Lambda} = 0.7$ is adopted throughout this paper.

2. Sample and Data

2.1. Sample Selection

The targets were drawn from the Calán-Tololo survey (Maza et al. 1996 and references therein), the 2dF QSO Redshift Survey (Croom et al. 2004), and the Hewitt–Burbidge QSO compilation (Hewitt & Burbidge 1989). They correspond to quasars of very high luminosity, typically $M_B \sim -29$ mag, located at the high-luminosity end of the quasar luminosity function (Bongiorno et al. 2007; Ross et al. 2013). A first spectroscopic run carried out in 2006 March with the du Pont telescope at Las Campanas Observatory (LCO) allowed us to corroborate their quasar nature and the presence of intense emission lines suitable for RM. At this redshift range, four lines are readily seen in the spectra of all our quasars: Ly α , Si IV, C IV, and C III].

Toward the end of the monitoring campaign, when confirming the redshift of CT252, we realized that the published value for this source (see Maza et al. 1993, where a redshift of 2.5 was provided) is much lower than the rest of the sample, at $z = 1.818$. This was probably because its very strong and nonsymmetric C IV line was mistakenly identified as Ly α . Hence, for this source Ly α is not visible in our spectra, but instead we can observe the Mg II emission line.

The redshifts for the quasars were obtained from our own data from the C III] line, except for CT320, where the line fit quality was poor. For this object the C IV redshift is reported instead. For CT252 the Mg II redshift is given. Redshifts are found in Table 1, together with some basic information for each quasar, such as the R -band magnitude, its standard deviation (see Section 3), and radio flux measurements (see below). SE virial masses are also reported using the calibration for the C IV emission line presented in Mejía-Restrepo et al. (2016). These were determined using our FWHM measurements of the C IV emission line. A virial factor f of 1 was assumed, which is appropriate for velocities estimated from FWHMs (e.g., Grier et al. 2017).

2.1.1. Spectral Properties

The mean spectra of each quasar can be seen in Figure 1. These have been flux-calibrated and corrected for Galactic extinction assuming the extinction law of Cardelli et al. (1989) and $R_V = 3.1$ in the observed frame. $E(B - V)$ values were in the range of 0.01–0.04 mag. For display purposes the spectra have been shifted in the vertical direction ordered by redshift (see caption for details). The absorption feature seen at the constant wavelength of $\sim 7600 \text{ \AA}$ corresponds to a telluric O₂ absorption. Rest-frame line luminosities, widths, and equivalent widths (EWs) are reported in Table 2.

Figure 1 shows a rather broad range of spectral properties, from objects with very broad lines, such as CT953 and J224743, to others with much narrower features, such as CT650 and J221516. Also, the lines can be very prominent (i.e., with large EW), like in the case of CT1061 and CT803, or rather weak (i.e., small EW), such as those in J002839 and J214355. The spectral shapes are rather uniform, with the exception of CT252, for which we are observing a very

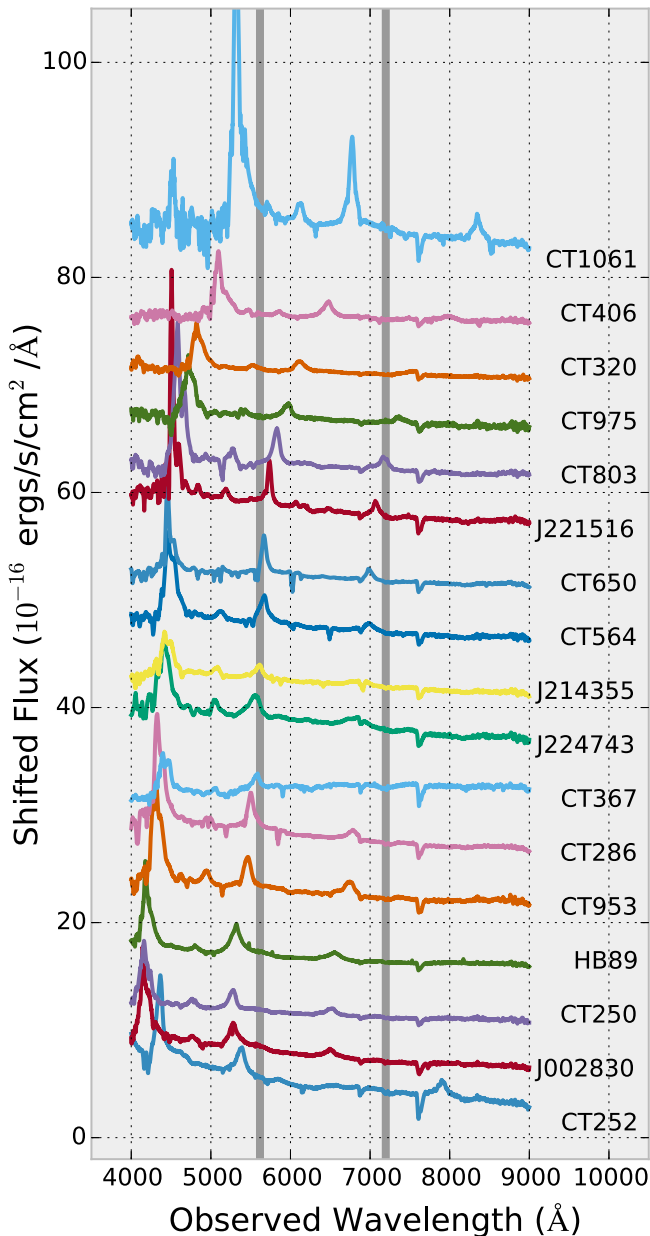


Figure 1. Flux-calibrated, Galactic-extinction-corrected, mean spectra of the 17 quasars reported in this work. The spectra have been shifted in the y-axis for display purposes, starting with a zero shift for CT252, five units of flux for J002830, 10 units of flux for CT250, and so on. The gray lines approximately demarcate the wavelength region corresponding to the *R*-band filter.

different spectral range in the rest frame, and CT367, which clearly shows a red spectral shape.

In between gray lines we highlight the 5620–7200 Å wavelength range, which roughly corresponds to the width of the *R*-band filter. Depending on the redshift of the source, the observed *R*-band 5620–7200 Å wavelength range corresponds to a mean rest-frame wavelength of 1465 Å for our highest-redshift source (CT1061), 1530 Å for our second-highest-redshift source (CT406), and 2271 Å for the lowest-redshift source (CT252). The remaining sources are found in the range 1620–1880 Å. It can be seen that this region of the spectra contains the C III] emission line, which, as we will see, does not show strong variability. However, for CT1061, CT320, CT406, CT564, CT650, CT803, CT975, and J221516 the C IV line is

redshifted into the *R*-band coverage. This could affect the analysis of the variability. However, the very broad nature of the *R* band and the small amplitude observed in the line variations secure a negligible interference: using the EW values presented in Table 2 and assuming a width of the *R*-band filter of 2200 Å, it can be seen that the total C IV line flux would contribute at most 10% to the observed-frame *R*-band photometry.

2.1.2. Radio-loudness and Spectral Energy Distributions

It is of interest to determine the radio-loudness of the quasars in our sample. Usually, a radio-to-optical flux ratio threshold of $R_{\text{radio}} = f(6 \text{ cm})/f(4400 \text{ Å}) = 10$ is adopted to separate radio-loud (RL) from radio-quiet (RQ) systems, while values between 10 and 100 are sometimes referred to as radio-intermediate. We searched two surveys for radio sources consistent with the positions of our quasars. First, the Sydney University Molonglo Sky Survey (SUMSS) Source Catalog (Mauch et al. 2003), which covers the southern sky for declinations $-50^\circ < \delta < -30^\circ$ at 843 MHz, reaches a depth of 6 mJy beam^{-1} and has a spatial resolution of $45 \times 45 / \cos(|\delta|)$ arcsec². We also searched the National Radio Astronomy Observatory Very Large Array Sky Survey (NVSS) catalog (Condon et al. 1998), which covers the sky north of -40° at 1.4 GHz, reaching a depth of $0.45 \text{ mJy beam}^{-1}$ and with a spatial resolution of $45''$. The presence of counterparts was confirmed by eye inspection of the radio maps. We *K*-corrected the radio measurements assuming a power-law spectral energy distribution of the form $S_\nu \propto \nu^{-\alpha}$, with index $\alpha = 0.75$ (Wang et al. 2007; Momjian et al. 2014).

To determine the rest-frame optical fluxes, we obtained *J*, *H*, and *K* magnitudes from the Two Micron All Sky Survey (2MASS) All-Sky Catalog of Point Sources (Cutri et al. 2003). No 2MASS photometry was available for CT250, CT286, or CT975. We also obtained fluxes at 5100 Å, applying the correlation between continuum emission at 1350 and 5100 Å found in Mejía-Restrepo et al. (2016), and extrapolating from our *R*-band photometry using the quasar rest-frame UV power-law index ($\alpha = 0.44$) obtained by Vanden Berk et al. (2001).

The spectral energy distributions for our sample are presented in Figure 2. It can be seen that in several cases there is good agreement between the spectra, their extrapolations to 5100 Å, and the 2MASS photometry. However, it is also seen that the extrapolation based on the work by Vanden Berk et al. (2001) is a factor of ~ 2 higher than that obtained applying the correlation found in Mejía-Restrepo et al. (2016), which in most cases falls below the 2MASS observations. The relation found in Trakhtenbrot & Netzer (2012) predicts fluxes about halfway between the two previous extrapolations. An anomalous case is CT650 (and perhaps CT803 and HB89), which was clearly brighter at the time of the 2MASS observations. CT367 has a spectral shape that is clearly poorly represented by the extrapolation to 5100 Å, while for J221516 the 2MASS photometry suggests an upturn of the 2MASS fluxes toward longer wavelengths. In summary, only for those objects without 2MASS photometry and CT650 will we use the spectral 5100 Å extrapolation based on Vanden Berk et al. (2001) to estimate the rest-frame optical flux. For all other objects, the 2MASS photometry will be adopted. The 5100 Å luminosities are reported in Table 1. To *K*-correct the observations to the rest-frame 4400 Å needed to determine

Table 2
Line Measurements

Quasar	Ly α			Si IV			C IV			C III]		
	L (erg s $^{-1}$)	EW (\AA)	FWHM (km s $^{-1}$)	L (erg s $^{-1}$)	EW (\AA)	FWHM (km s $^{-1}$)	L (erg s $^{-1}$)	EW (\AA)	FWHM (km s $^{-1}$)	L (erg s $^{-1}$)	EW (\AA)	FWHM (km s $^{-1}$)
CT1061	2.1e+46	64	3355	2.4e+45	10	4843	8.9e+45	44	3218	1.4e+45	9	2452
CT250	2.1e+46	64	3355	2.4e+45	10	4843	8.9e+45	44	3218	1.4e+45	9	2452
CT286	2.5e+45	57	6817	3.3e+44	10	6676	1.0e+45	35	6256	3.6e+44	17	5900
CT320	1.3e+45	13	2934	2.8e+44	4	5312	7.8e+44	11	3493	2.3e+44	5	3796
CT367	2.0e+45	33	5368	3.9e+44	9	6453	1.2e+45	33	6844	1.4e+44	5	2085
CT406	1.2e+45	23	4869	1.9e+44	5	3922	1.7e+45	40	6236	2.1e+44	4	8828
CT564	3.8e+45	46	4943	3.8e+44	7	4814	1.8e+45	35	5623	5.9e+44	17	6361
CT650	4.1e+45	52	7007	4.3e+44	6	6053	6.1e+44	10	3419	4.9e+44	12	8593
CT803	1.4e+45	20	2266	1.4e+44	3	3029	1.1e+45	21	3437	6.7e+44	18	4009
CT953	7.3e+45	107	5506	8.0e+44	13	5044	3.1e+45	54	5005	3.4e+44	7	7929
CT975	4.2e+45	47	8199	6.6e+44	10	5875	2.3e+45	40	5970	3.1e+44	7	4468
HB89 0329–385	9.5e+44	14	6275	2.9e+44	5	5231	1.1e+45	22	5831	6.6e+44	19	4070
2QZ J002830	2.4e+45	46	3975	1.7e+44	4	5603	1.9e+45	57	7326	6.7e+44	28	8336
2QZ J214355	1.6e+45	19	4397	2.8e+44	5	6342	7.9e+44	15	6895	3.5e+44	9	4360
2QZ J221516	1.1e+45	15	5857	3.4e+44	6	5239	9.4e+44	17	5888	1.4e+44	4	2893
2QZ J224743	5.0e+45	41	2410	4.8e+44	5	4419	2.2e+45	25	2728	6.5e+44	10	2966
	1.0e+45	10	5206	5.1e+44	6	4685	1.9e+45	23	8861	1.1e+44	2	2010

Quasar	C IV			C III]			Mg II		
	L (erg s $^{-1}$)	EW (\AA)	FWHM (km s $^{-1}$)	L (erg s $^{-1}$)	EW (\AA)	FWHM (km s $^{-1}$)	L (erg s $^{-1}$)	EW (\AA)	FWHM (km s $^{-1}$)
CT252	1.4e+45	28	5198	2.7e+44	7	4970	4.9e+44	16	3800

Note. Measurements were obtained from the mean spectrum of each source in the rest frame.

R_{radio} , the Vanden Berk et al. (2001) spectral index was again used.

The results on the radio-loudness are reported in Table 1. Three sources were found to be radio-loud quasars: CT286, HB89, and J221516 ($R_{\text{radio}} = 48 \pm 10$, 50 ± 9 , and 576 ± 100 , respectively), the last two already noticed as radio-loud systems in the literature (Shemmer et al. 2004; Chhetri et al. 2013). The remaining objects are split into 12 secure RQ systems and two with upper limits above $R_{\text{radio}} = 10$ (CT250 and CT650). Leaving these two last sources aside, a fraction of 3/15 radio-loud quasars is found, which is in good agreement with the general quasar population at the high end of the luminosity range (Cirasuolo et al. 2003).

2.2. Broadband Imaging

Photometric monitoring of ~ 50 high- z AGNs started in 2005 February. After a few years, the less variable systems were dropped, and we continue to monitor $\sim 60\%$ of the original sample. The data were obtained with the 1.3 and 0.9 m SMARTS telescopes using broadband R imaging. Several observations per year were acquired in queue mode. The light curves reported in this work extend until 2017 January.

Bias subtraction and flat correction were done in the usual way using IRAF tasks. PSF differential photometry of the quasars was obtained using typically 10–12 local stars. The stars were in turn calibrated against their R -band USNO magnitudes so that the light curves are finally expressed in flux units. Formal photometric errors for the stars were generally small. Therefore, a 0.015 mag error, as obtained from the median standard deviation of the observed stellar fluxes, was adopted as a more representative photometric error.

2.3. Spectroscopy

To secure an accurate relative spectrophotometric calibration, we followed Maoz et al. (1990) and Kaspi et al. (2000) and rotated the spectrograph so that the quasar and a comparison star are observed through the same slit. The WFCCD at the du Pont telescope at LCO proved to be a very reliable instrument, allowing us to position the quasar and comparison star within the slit with subpixel precision, for a pixel size of $0''.484$. The slit width was 8.1 arcsec wide throughout the observations.

The spectroscopic monitoring started in 2007 April, and the latest data were obtained in 2017 January. We aimed at having at least one observation per year for each quasar, although weather and instrumental problems sometimes did not allow us to fulfill this goal. Typically each observation consisted of three repeated spectra of 900–1200 s of exposure time. The spectra were reduced in the standard way using IRAF tasks: bias subtraction and flat calibration were applied using bias frames and internal lamps observed each night. Flats were obtained using the same wide slit as the science frames. One-dimensional spectra of the quasar and comparison star were extracted using the same fixed aperture along the spectral direction. Wavelength calibration was determined using helium, neon, and argon calibration “arcs” obtained using a narrow slit.

To achieve the relative spectrophotometry, the spectrum of each quasar was divided by the heavily smoothed spectrum of the simultaneously observed comparison star, and then the separate “normalized-quasar spectra” were combined. To secure a homogeneous wavelength calibration around the Ly α , Si IV, C IV, and C III] emission lines (and Mg II in the case of CT252), sections of the spectra around each line were used

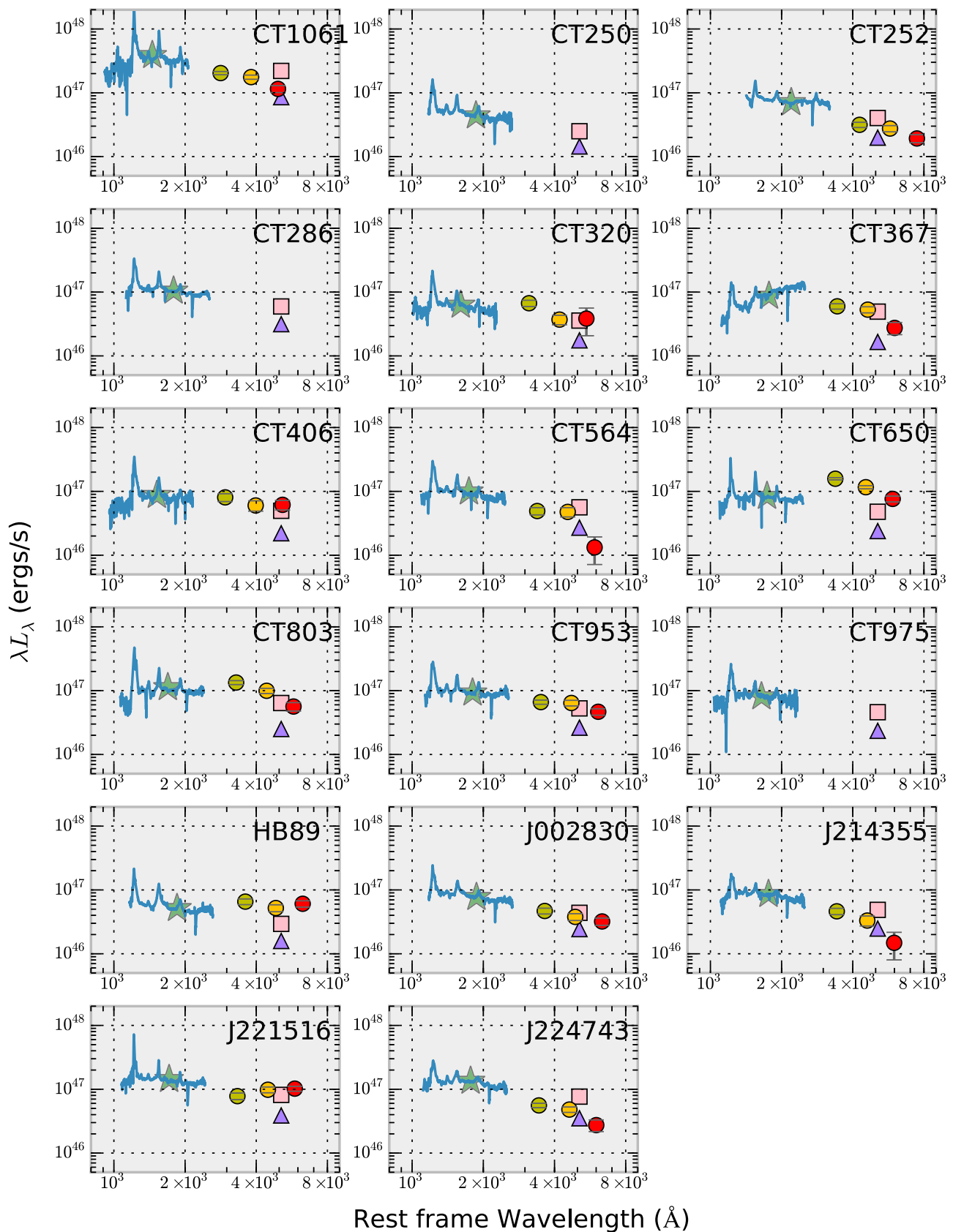


Figure 2. Rest-frame spectral energy distributions of the quasars in our sample. Mean spectra for each source are shown together with our *R*-band (stars) and *JHK* 2MASS (circles) photometry. Two extrapolations to 5100 Å are also included: from 1350 Å (triangles) using the correlation determined in Mejía-Restrepo et al. (2016), and from the *R*-band photometry (squares) using the UV power-law index determined by Vanden Berk et al. (2001).

CT650

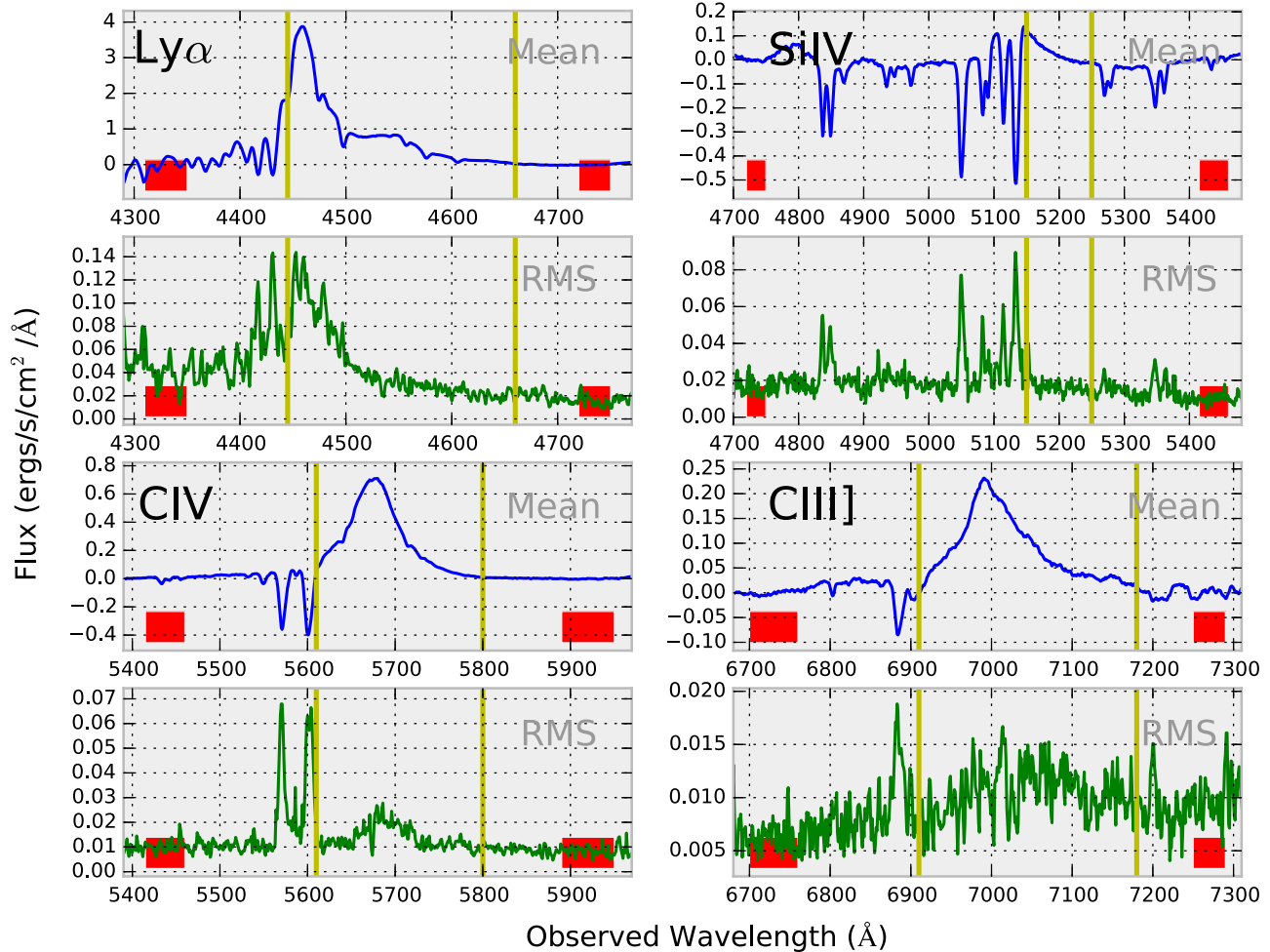


Figure 3. Mean (top panels—in blue) and rms (bottom panels—in green) spectra of CT650 around the Ly α , Si IV, C IV, and C III] emission lines. The mean spectra have been continuum-subtracted using the continuum measurements obtained at the positions marked by red boxes. The line measurement is obtained as the summation of all flux between the vertical yellow lines.

to perform a cross-correlation analysis. The spectra were then shifted according to the cross-correlation results. This was particularly important at the blue end of the spectra, where only a few lines from the comparison arcs were available, thus making the wavelength solution rather unreliable.

Line flux measurements were obtained by adopting two small pseudo-continuum windows located at each side of the corresponding emission line. The continuum level under the line in consideration was then assumed to correspond to the interpolation of a straight line joining the mean flux obtained from the pseudo-continuum windows. We checked that the pseudo-continuum windows corresponded to regions with small values in the rms spectrum of each quasar to avoid the presence of weak emission or absorption lines. Likewise, to avoid introducing a spurious line variability signal due to variations of strong self-absorbing features, we limited the line flux measurements to regions devoid of absorption lines, which were readily seen in the rms spectra. As an example, Figure 3 shows the mean and rms spectra for the emission lines in the quasar CT650. The placement of the continuum windows and the region adopted for the line flux measurements are shown. As can be seen, Si IV is heavily absorbed throughout the profile, while the remaining lines show strong and variable

absorption in their blue wings. Hence, the line fluxes were determined to the right of Ly α , C IV, and C III], while the light curve of the Si IV was obtained from a small spectral window. Notice, however, that if nonvariable absorption profiles are present in the line profiles, we do not make any attempt to isolate them from the line flux measurements.

Errors in emission-line measurements were estimated assuming that the line flux L can be expressed as $L = \alpha(F - C)$, where α is the scaling by the division of the comparison star, F is the total flux measured in the regions defined for line flux measurement (i.e., between the yellow vertical lines shown in Figure 3), and C is the interpolated continuum as defined above. Hence, the variance for each line measurement can be written as $\sigma_\alpha^2(F - C)^2 + \alpha^2(\sigma_F^2 + \sigma_C^2)$, where σ denotes uncertainty in the quantity given by the subscript.

To estimate σ_α , which encompasses effects such as poor centering of the quasar–star pair on the slit or guiding problems, we determined the ratio of two normalized-quasar spectra obtained during a single observing run. Since typically three observations were obtained per night, two such ratios could be constructed per quasar observation. The ratio distribution using all available data for all quasars can be seen

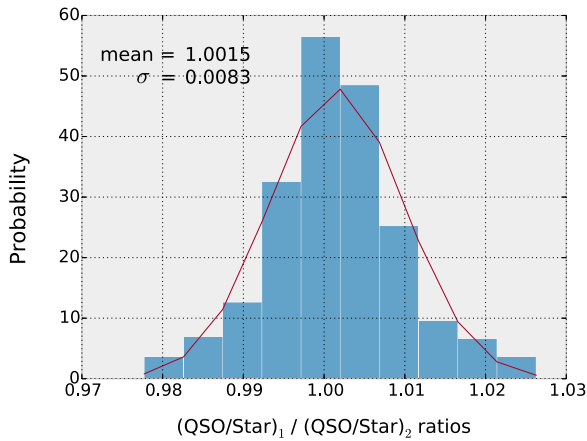


Figure 4. Distribution of quasar/star ratios.

in Figure 4, where the mean and standard deviation of the distribution are also given.

To estimate σ_F , we used the error spectrum of each quasar observation (which is obtained assuming photon Poisson statistics and the specific gain and readout noise of the detector) and determined the total variance as the quadratic sum of the errors from each pixel within the line window. During this step, we did not take into account the division by the comparison star, as their spectra were heavily smoothed before the division and therefore introduced no further noise.

Finally, to estimate σ_C , we resorted to Monte Carlo (MC) simulations because of the rather complex uncertainties that the determination of the continuum level might introduce. For example, continuum window placement can be affected by small mismatches in the wavelength solution, which, in turn, will impact the flux measurement in regions with strong flux fluctuations, like toward the blue end of the spectra. This is particularly true for the Ly α pseudo-continuum windows, since the normalized-quasar continuum flux can increase sharply because of the division by a comparison star with a spectral energy distribution that falls quickly toward the blue. The Ly α blue pseudo-continuum window is also affected by the shape of the continuum owing to intergalactic absorption.

We obtained 10,000 MC realizations for each line measurement where the flux level in each pseudo-continuum window was determined using fluxes drawn from a Gaussian distribution around the observed window flux values. For the standard deviation of the distribution we adopted the largest value between the flux rms within the pseudo-continuum window and the photon noise derived from the error spectrum within the same window. As expected, for Ly α the flux rms was consistently larger than the photon noise. The determined flux distributions were then normalized and integrated from the ends to a cumulative value of 0.159 (i.e., corresponding to a 1 σ confidence limit). σ_C was adopted as half the range given by these two limits.

We found that all three terms of the variance, $\sigma_\alpha^2(F - C)^2$, $\alpha^2 \sigma_F^2$, and $\alpha^2 \sigma_C^2$, were comparable and necessary to have a full description of the emission-line flux errors.

To increase the number of continuum measurements available for the variability analysis, we measured the mean value of the continuum in the 5620–7200 Å wavelength range from each spectroscopic observation, as a proxy for R -band photometric values. These “spectroscopic” points were later scaled to the broadband R -band photometry using a simple χ^2

minimization to bring the mean “spectroscopic” light curve in line with the photometric values.

R -band, Ly α , Si IV, C IV, and C III] light curves are presented in Figure 5 for all objects except for CT252, for which C IV, C III], and Mg II light curves are presented. The full database is found in the Appendix.

3. Variability Analysis

3.1. General Continuum and Emission-line Variability

Here we report on the ~ 10 yr observer-frame light curves for 17 quasars with spectroscopic follow-up. The variability properties for these observations are reported in Table 3. We list the number of epochs available (with the R band counting both the broadband and spectroscopic continuum measurements); R_{\max} , the ratio between the maximum and minimum flux; f_{var} , the normalized variability amplitude $(\sqrt{\sigma^2 - \delta^2})/\bar{f}$, where δ are the photometric uncertainties, \bar{f} is the light-curve mean flux, and σ is its standard deviation; Rodríguez-Pascual et al. 1997); χ^2 , the reduced chi-square fit to a model with constant flux; P_χ , the probability that the observed χ^2 is due to random errors; and cc, which indicates whether lag determination between emission-line and continuum light curves was obtained (see Section 4). Formally, a source is considered variable if $P_\chi > 0.95$ and $\bar{f} > 0$. Notice, however, that these statistical descriptions deal with the amplitude of the variability only, and not with the structure of the light curves as a function of time. In other words, while the errors in some light curves are consistent with no variations, the shape of the light curve might suggest a systematic flux change with time. This is particularly important for the emission-line light curves, where errors are difficult to quantify properly. This can be appreciated, for example, in the Ly α light curve of CT1061, which has a $P_\chi = 0.4$ and $\bar{f} = 0$ but shows a clear trend of decreasing flux as a function of time.

From Table 3 it can be seen that all R -band light curves show significant variability and have $P_\chi = 1.0$ and $\bar{f} > 0$. Still, there is a range of properties in the variability structure, with some sources presenting very smooth, slowly varying fluxes (e.g., CT367), while others go through epochs of more random, fast-changing fluxes (e.g., CT320).

Most emission-line light curves present significant variability. Adopting $P_\chi \geq 0.95$ for variable light curves, 15/17 quasars show large Ly α flux fluctuations. C IV follows with 12/17, Si IV with 10/17, and C III] with 12/17 (plus Mg II with 1/1 for CT252). In summary, we find that Ly α presents a very high probability of showing strong variability. This is in contrast to previous results that detected no variations in this line for high-luminosity sources (Ulrich et al. 1993; Kaspi et al. 2007). C IV is also a highly variable line, followed by Si IV and C III]. This is expected, as these lines are generally weaker, and therefore it becomes harder to determine statistically significant variations. It should be noticed, however, that our spectroscopic sample was selected as those quasars that showed significant R -band variability, and therefore it could be biased toward highly variable sources. Comparison with previous experiments might therefore not be very meaningful.

In what follows we divide our sample into two groups: a first group with “expected” line variability (14/17), i.e., those showing emission-line light curves that agree with the expectations given the continuum variations, and a second group of those objects with detected line variability that seem

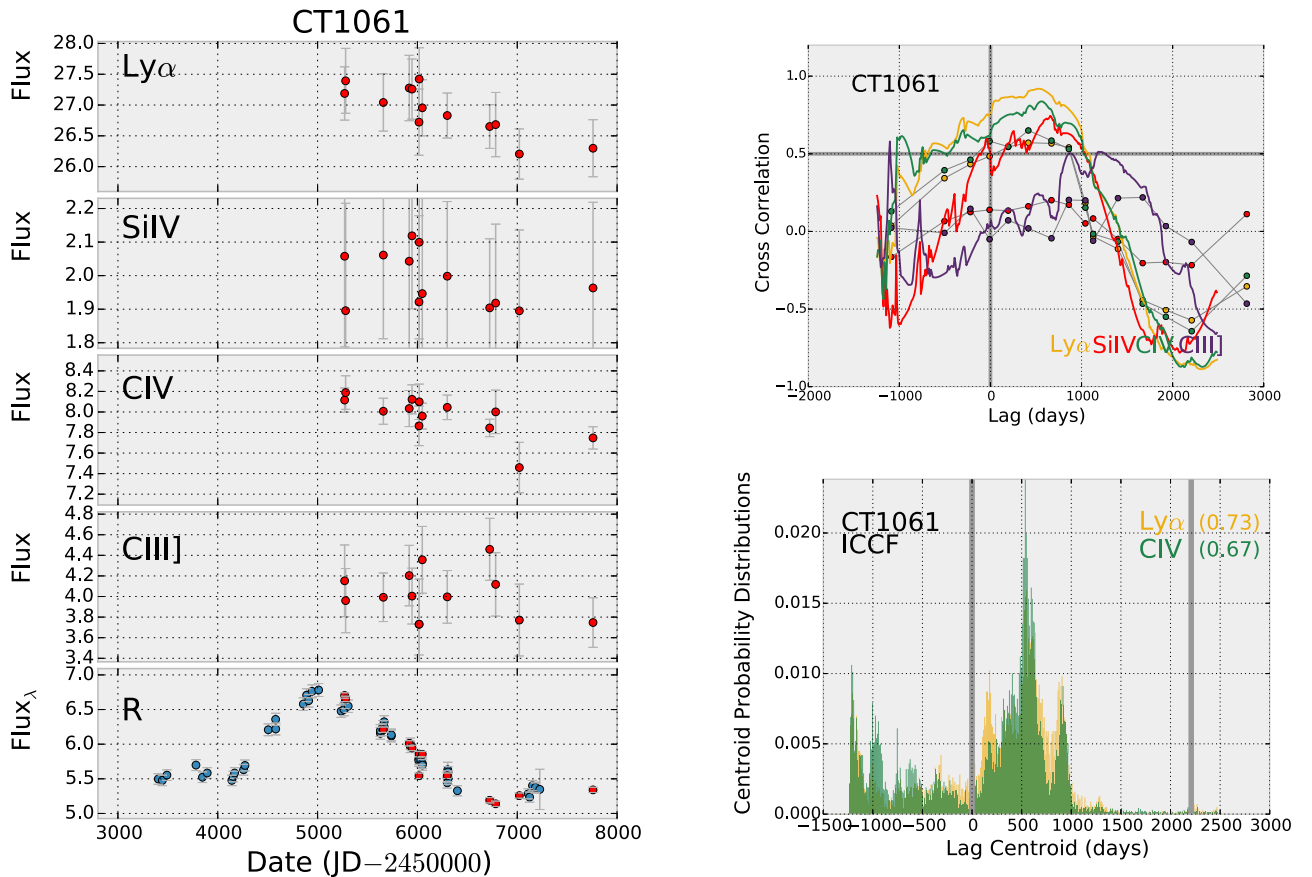


Figure 5. Left: line and continuum light curves for all quasars with spectroscopic follow-up. Red circles correspond to measurements taken from the spectroscopic data, while blue circles correspond to broadband R photometry. Units are 10^{-14} erg s^{-1} cm^{-2} for the line measurements and 10^{-16} erg s^{-1} cm^{-2} \AA^{-1} for the R-band light curves. Top right panels: correlation functions obtained using the ICCF (solid line) and ZDCF (circles) methods for the Ly α , Si IV, C IV, and C III] emission lines. Bottom right panels: CCCDs obtained from the ICCF FR/RSS analysis for those lines with significant peaks in their ZDCF and ICCF correlation functions. Thick gray lines show the limits of the distributions used for lag error determinations. The fraction of the CCCD contained within the thresholds is shown in parentheses for each line. For further details, see the text.

(The complete figure set (17 images) is available.)

to respond to the continuum changes in unexpected ways (3/17).

3.2. Quasars with Expected Line Response

Most of the monitored quasars show some degree of line variation that mimics the continuum variability after some elapsed time (see left panels in Figure 5). This is crucial for the cross-correlation analysis presented in Section 4, as quasars in this group show good indication that the emission lines are reverberating as a response to variations in the continuum. Unfortunately, some sources in this group present rather monotonic flux variations (CT367, CT803, J002830), and therefore the present light curves are not suitable for cross-correlation analysis. This will be further characterized in Section 4.

3.3. Quasars with Unexpected Line Response

We find three quasars where the line responses to the continuum variations are hard to interpret. These are CT320, CT803, and J224743.

In all sources one of the emission lines seems to have disengaged from the observed continuum, while the remaining lines show a pattern of variability more consistent with the

R-band light curve. In the case of CT320, the anomalous behavior is observed in Si IV, while for CT803 and J224743, it is observed in Ly α . As we will see in Section 4, very little correlation is observed in the cross-correlation analysis of the light curves in these emission lines.

The most likely explanation for the lack of correlation between continuum and line emission light curves is that in these objects the *observed* continuum is not a good counterpart of the ionizing continuum responsible for the observed line variations. This is not completely unprecedented, as we will further see in the discussion section.

4. Cross-correlation Analysis

Cross-correlation functions (CCFs) for all our targets with spectroscopic data were determined. All emission-line light curves are used, irrespective of their P_{χ} values, since, as we have seen, this quantity does not reflect the structure of the variability.

Three methods were employed to examine the degree of correlation between the continuum and emission-line light curves: the interpolated cross-correlation function (ICCF, e.g., Peterson et al. 1998, 2004), the z -transformed discrete correlation function (ZDCF) as defined by Alexander (1997), and the JAVELIN method described by Zu et al. (2011, 2013).

Table 3
Light-curve Variability Statistics

Quasar	l.c.	N	R_{\max}	f_{var}	χ^2	P_{χ}	cc	Quasar	l.c.	N	R_{\max}	f_{var}	χ^2	P_{χ}	cc
CT1061	Lya	13	1.05	0.00	0.8	0.30	y	CT803	Lya	21	1.15	0.02	2.0	1.00	n
	Si IV	13	1.12	0.00	0.1	0.00	n		Si IV	21	1.31	0.05	3.0	1.00	n
	C IV	13	1.10	0.01	1.4	0.83	y		C IV	21	1.15	0.00	0.5	0.04	n
	C III]	13	1.20	0.00	0.6	0.14	n		C III]	21	1.26	0.00	0.6	0.06	n
	R	65	1.32	0.08	56.8	1.00	...		R	79	1.47	0.08	50.3	1.00	...
CT250	Lya	17	1.22	0.05	11.9	1.00	y	CT953	Lya	23	1.35	0.07	11.4	1.00	y
	Si IV	17	1.54	0.00	1.0	0.58	y		Si IV	23	1.71	0.08	3.9	1.00	y
	C IV	17	1.39	0.06	4.7	1.00	y		C IV	23	1.27	0.05	5.4	1.00	y
	C III]	17	1.40	0.03	2.0	0.99	n		C III]	23	1.21	0.00	1.3	0.82	n
	R	67	1.47	0.11	81.1	1.00	...		R	74	1.61	0.12	592.3	1.00	...
CT252	C IV	17	1.25	0.07	34.4	1.00	n	CT975	Lya	17	1.20	0.03	1.6	0.94	n
	C III]	17	1.10	0.01	1.3	0.78	n		Si IV	17	2.73	0.00	0.9	0.49	n
	Mg II	17	1.49	0.09	15.6	1.00	n		C IV	17	1.33	0.05	2.4	1.00	n
	R	62	1.41	0.07	962.7	1.00	...		C III]	17	2.70	0.12	2.8	1.00	n
									R	63	1.94	0.12	86.5	1.00	...
CT286	Lya	23	1.20	0.04	8.8	1.00	y	HB89 0329–385	Lya	22	1.31	0.05	7.1	1.00	y
	Si IV	23	1.36	0.00	0.5	0.04	y		Si IV	22	1.91	0.00	0.9	0.43	y
	C IV	23	1.25	0.04	2.5	1.00	y		C IV	22	1.09	0.00	1.4	0.88	n
	C III]	23	1.16	0.00	0.4	0.01	n		C III]	22	1.21	0.00	0.9	0.40	y
	R	85	1.46	0.10	572.7	1.00	...		R	68	1.38	0.09	288.0	1.00	...
CT320	Lya	26	1.19	0.04	14.9	1.00	y	2QZ J002830	Lya	9	1.22	0.06	27.9	1.00	n
	Si IV	26	1.57	0.10	5.6	1.00	y		Si IV	9	1.53	0.11	5.9	1.00	n
	C IV	26	1.21	0.04	8.6	1.00	y		C IV	9	1.27	0.07	21.0	1.00	n
	C III]	26	1.32	0.05	5.8	1.00	y		C III]	9	1.14	0.03	2.0	0.96	n
	R	74	1.53	0.10	167.3	1.00	...		R	54	1.64	0.11	98.7	1.00	...
CT367	Lya	12	1.19	0.04	18.3	1.00	n	2QZ J214355	Lya	16	1.21	0.00	0.9	0.41	y
	Si IV	12	2.64	0.24	94.1	1.00	n		Si IV	16	1.33	0.00	0.5	0.08	n
	C IV	12	1.12	0.03	5.6	1.00	n		C IV	16	1.33	0.03	2.5	1.00	n
	C III]	12	1.25	0.05	4.5	1.00	n		C III]	16	1.60	0.00	0.3	0.00	n
	R	66	1.85	0.19	224.7	1.00	...		R	64	1.35	0.07	439.0	1.00	...
CT406	Lya	15	1.10	0.03	8.3	1.00	y	2QZ J221516	Lya	21	1.14	0.03	19.9	1.00	y
	Si IV	15	1.52	0.10	3.6	1.00	n		Si IV	21	1.56	0.05	1.2	0.78	n
	C IV	15	1.25	0.04	4.4	1.00	y		C IV	21	1.16	0.03	2.9	1.00	y
	C III]	15	2.52	0.12	6.5	1.00	n		C III]	21	1.36	0.00	0.9	0.43	n
	R	62	1.39	0.07	59.5	1.00	...		R	78	1.34	0.08	110.1	1.00	...
CT564	Lya	12	1.15	0.04	11.5	1.00	y	2QZ J224743	Lya	17	1.46	0.11	76.3	1.00	n
	Si IV	12	4.21	0.11	1.2	0.70	n		Si IV	17	1.52	0.11	12.5	1.00	n
	C IV	12	1.19	0.02	1.7	0.93	y		C IV	17	1.11	0.00	1.7	0.96	n
	C III]	12	1.46	0.00	0.7	0.25	n		C III]	17	1.20	0.01	2.1	0.99	n
	R	66	1.45	0.10	74.9	1.00	...		R	60	1.29	0.05	55.2	1.00	...
CT650	Lya	25	1.17	0.03	70.5	1.00	y								
	Si IV	25	7.66	0.29	13.8	1.00	n								
	C IV	25	1.14	0.03	41.4	1.00	y								
	C III]	25	1.27	0.06	39.8	1.00	y								
	R	76	2.03	0.15	176.7	1.00	...								

We will discuss cross-correlation results for the ICCF and ZDCF methods first, which are presented in the top right panels of Figure 5, and later comment on the JAVELIN findings.

The ICCF determines the maximum of the CCF between light curves after interpolating fluxes to a desired cadence. The assumption used is that the line and continuum fluxes in gaps between two observed points are properly approximated by a linear interpolation in time between the two (see, e.g., Peterson et al. 2004, and references therein). For our sample, the ICCF was run for a cadence of 10 days and between $-s/2$ and s days, where s is the time span common to the continuum and each emission-line light curve.

Of the three cross-correlation methods described here, ZDCF is the only one that works solely with the *observed* values of the light curves. It is based on the discrete correlation function (DCF) of Edelson & Krolik (1988), which uses the available

data without resorting to interpolation, hence not altering the observed light curves. The DCF method bins the time difference pairs and obtains the mean correlation coefficient for each bin. A minimum of 11 points is required in each bin, which determines the length of the correlation, except for the two bins at the edges, where a smaller number of points are allowed. The ZDCF introduces a “z-transformation” of the DCF correlation coefficient in order to avoid the inherent skewedness of the DCF parent distribution function.

Inspection of the correlations presented in the top right panels of Figure 5 shows that in some cases the ICCF and ZDCF follow each other closely (e.g., Ly α and C IV in CT250), while in other cases there are significant differences (e.g., Si IV in CT250 and all lines for J214355), with the ICCF showing higher correlation coefficients than the ZDCF. This is due to the “extra” information introduced by the interpolation

technique. Also, in some cases the ICCFs are more extended than the ZDCF (e.g., CT406), because of the requirement of a minimum number of points per bin by the ZDCF. In other words, those regions where the ICCFs extend further than the ZDCFs correspond to regions of sparsely sampled light curves. In summary, ZDCF results give a more conservative inference of the correlation strength.

Given the above differences between the methods, we will only consider those emission-line light curves that have ICCF and ZDCF cross-correlation coefficient distributions agreeing with each other and a well-defined peak for positive lags above a cross-correlation coefficient of 0.5 (this is at least one ZDCF point above 0.5, which is part of a coherent peak seen in the ZDCF; usually the ICCF will be found at even higher correlation coefficient levels). We treat negative peaks as a failure to determine physical meaningful lags, although different explanations, involving a whole different view of the central region of AGNs, could also be considered. Hence, the peaks to be considered should be found in the upper right quarter of the top right panels of Figure 5. For example, we will consider the Ly α and C IV light curves for CT1061 but drop the Si IV and C III] light curves of this source.

Following these criteria, we drop CT252, CT367, CT803, J002830, and J224743 from any further analysis. For the remaining sources not all emission lines will be considered. This is indicated in Table 3.

To estimate the lags, the maximum of the ICCF can be determined in two ways: finding the peak (or maximum value) of the ICCF (for positive lags and cross-correlation coefficients larger than 0.5), and finding its centroid (or weighted mean) around the peak above a certain threshold value. As centroids are more reliable than peaks in flat or noisy ICCFs, in what follows we adopt the centroids (τ_{cent}) as the measured lags for those sources showing significant ICCF and ZDCF peaks, as discussed above. In our case, for the determination of τ_{cent} , a threshold of 0.85 times the maximum was used.

To determine the lag-associated errors, we followed the usual flux randomization and bootstrapping MC technique (also known as FR/RSS), using a code facilitated by B. Peterson. Briefly, ICCFs are computed from light curves constructed after fluxes are randomized within the observed errors (flux randomization—FR), and 70% of points are selected from the observed sequences (random subset selection—RSS)—for more details see Peterson et al. (1998, 2004). A total of 10,000 such trials were obtained. As before, the trials had a cadence of 10 days and run between $-s/2$ and s days. With all successfully determined centroids, cross-correlation centroid distributions (CCCDs) for objects showing significant ICCF and ZDCF peaks are presented in the bottom right panels of Figure 5.

CCCDs in Figure 5 show a wide range of morphologies, with sometimes more than one peak of high statistical probability. This is in contrast to the CCCDs obtained for many well-monitored Seyfert galaxies, since the presence of many variability “events” helps to constrain the lags to a singular, well-defined peak (see, e.g., Clavel et al. 1991; Wanders et al. 1997; Peterson et al. 2005; Edelson et al. 2015; Fausnaugh et al. 2016). This degeneracy in the possible lags seen in the bottom right panels of Figure 5 cannot be unambiguously solved unless the light curves could be dramatically extended in duration. However, it is clear that the observed secondary peaks are found at the same locations

where unfeasible peaks were also observed in the ICCF-ZDCF distributions shown in the top right panels of Figure 5 (i.e., regions where the number of ZDCF points is small and hence the ICCF interpolation is not very meaningful; see below). Therefore, we can use the same arguments as before to dismiss them.

For the lag error determinations we truncated the CCCDs at a minimum and maximum lag and renormalized. The criteria were to leave out complete peaks that implied negative lags (which are unfeasible), while negative wings of positive lags were still taken into account. The upper threshold was given by the largest time bin computed by the ZDCF algorithm before the final bin (which usually has less than 11 measurements), i.e., before the light curves become too sparse for meaningful interpolation and lag determinations. These thresholds are shown in Figure 5 using vertical gray lines. Lag errors were finally computed as a 1σ confidence limit range by integrating the renormalized CCCDs from the determined thresholds until a cumulative value of 0.159 was reached on each end, which determines σ_- and σ_+ . A final criterion to consider a lag as reliable is imposed at this stage, with the requirement that at least 50% of the original CCCD is found within the defined thresholds (see also Grier et al. 2017). This fraction is shown in each CCCD presented in Figure 5. This restriction leaves out the Mg II lag for CT252, the C III] lag for CT953, and the C IV lag for CT975. As before, this is indicated in the “cc” column in Table 3. Table 4 presents the final list of lags and their error estimates. The Mg II lag for CT252, C III] lag for CT953, and C IV lag for CT975 are also included in Table 4 but not used for further analysis.

We also used JAVELIN to characterize the observed lags (Zu et al. 2011, 2013). JAVELIN models the light curves as a damped random walk process (DRWP, also called the purely Auto-Regressive, AR(1), process) as prescribed by Kelly et al. (2009), i.e., assumes a particular regime of the power spectral function (with $P_i \propto \nu^\alpha$ with $\alpha = -2$, breaking to $\alpha = 0$ at a characteristic frequency) in order to determine a lag and its significance.

The advantage of JAVELIN over the ICCF method is that the errors associated with values interpolated between actual observations are based on the DRWP model, which are usually larger and more realistic than those obtained from a linear interpolation. However, for sufficiently well sampled light curves, it has been found that a DRWP model only applies to about half of AGNs of Seyfert and quasar-like luminosities (Kasliwal et al. 2015). Moreover, the basic assumption of JAVELIN is that the emission-line light curves are the result of the response to an ionizing continuum that is changing exactly in the same way as the observed continuum used in the calculations, in contradiction to some well-documented previous results (Goat et al. 2016), as well as some of the cases presented in this work. In fact, JAVELIN computes a solution that assumes a transfer function of the continuum and solves simultaneously for both, the continuum and line emission interpolated light curves.

We ran JAVELIN using the same lag limits used during the ICCF calculations, implemented 5000 Markov chain MC iterations during the “burn-in” phase and 10,000 iterations during the final parameter determination step, assumed the default models for the description of the continuum (DRWP, or “Cont_Model” in JAVELIN language) and line (“RMap_Model”) light curves, and solved for single continuum–line

Table 4
Cross-correlation Analysis

	Ly α				Si IV			
	τ_{cent} (days)	σ_- (days)	σ_+ (days)	M_{BH} ($10^9 M_{\odot}$)	τ_{cent} (days)	σ_- (days)	σ_+ (days)	M_{BH} ($10^9 M_{\odot}$)
CT1061	431 (99)	239 (55)	461 (106)
CT250	37 (11)	65 (19)	155 (45)	...	174 (51)	652 (191)	988 (290)	...
CT286	1191 (335)	78 (22)	542 (153)	0.6 ± 0.2	427 (120)	205 (58)	395 (111)	0.7 ± 0.5
CT320	-222 (-56)	105 (26)	365 (92)	...	1818 (459)	105 (26)	345 (87)	3.9 ± 0.6
CT406	16 (5)	105 (29)	505 (141)
CT564	426 (102)	193 (46)	647 (155)
CT650	548 (150)	54 (15)	56 (15)	0.16 ± 0.02
CT953	465 (127)	193 (53)	87 (24)	1.8 ± 0.6	779 (213)	637 (174)	1153 (315)	...
CT975
HB89	1543 (438)	171 (48)	399 (113)	1.4 ± 0.3	349 (99)	147 (42)	693 (196)	...
J214355	724 (187)	469 (121)	161 (42)	1.3 ± 0.6
J221516	637 (185)	43 (13)	147 (43)	0.22 ± 0.04
	C IV				C III]			
	τ_{cent} (days)	σ_- (days)	σ_+ (days)	M_{BH} ($10^9 M_{\odot}$)	τ_{cent} (days)	σ_- (days)	σ_+ (days)	M_{BH} ($10^9 M_{\odot}$)
CT1061	397 (91)	105 (24)	485 (111)
CT250	-24 (-7)	184 (54)	356 (104)
CT286	1629 (459)	327 (92)	253 (71)	1.1 ± 0.2
CT320	217 (55)	333 (84)	67 (17)	...	162 (41)	169 (43)	451 (114)	...
CT406	411 (115)	310 (86)	230 (64)	0.7 ± 0.5
CT564	419 (100)	106 (25)	674 (161)
CT650 ^a	592 (162)	38 (10)	122 (33)	0.4 ± 0.1
CT953 ^b	256 (70)	204 (56)	406 (111)	...	417 (114)	445 (122)	1355 (370)	...
CT975 ^b	289 (77)	33 (9)	157 (42)	0.5 ± 0.2
HB89	343 (97)	311 (88)	449 (127)	...
J214355	493 (128)	318 (82)	352 (91)	0.9 ± 0.6
J221516	566 (165)	43 (13)	337 (98)	0.3 ± 0.1
	Mg II							
	τ_{cent} (days)	σ_- (days)	σ_+ (days)	M_{BH} ($10^9 M_{\odot}$)				
CT252 ^b	550 (190)	170 (59)	330 (114)	...				

Notes. Lags are given in days in the observed frame and, in parentheses, in the rest frame. Black hole virial masses are given assuming a virial factor of 1. M_{BH} values are presented only for objects where $\tau_{\text{cent}}/\sigma_- > 1$ and $\tau_{\text{cent}}/\sigma_+ > 1$.

^a Centroid calculations for the CT650 C IV line failed in 60% of the trials.

^b The Mg II lag for CT252, C III] lag for CT953, and C IV lag for CT975 are not considered reliable, as they were obtained from less than 50% of the original CCD distributions.

pairs at each time. Figure 6 presents the JAVELIN lag posterior distributions for the same sources presented in Figure 5.

Comparison between the histograms presented in Figures 5 and 6 shows that both methods roughly agree on the best-determined lags. However, JAVELIN tends to present considerably compact probability distributions for most objects, in some cases with several well-defined, extremely narrow peaks. As already observed by Fausnaugh et al. (2016), this is mostly because of the very strong—and seldom demonstrated—assumption that the emission-line light curves are a simple lagged and smoothed version of the continuum emission. In fact, Fausnaugh et al. (2016) suggest that the actual dispersion is within 2σ – 3σ of the JAVELIN-quoted errors. In a few cases (e.g., CT1061), the JAVELIN results are very close to those found by our ICCF analysis.

JAVELIN results do not show spurious peaks at the edges of the probability distributions, which is also a consequence of the assumption of a BLR responding to the continuum light curves. Finally, it is interesting to notice some cases with contradicting results between the methods. For example, JAVELIN fails to determine an Mg II lag for CT252, while the ICCF method detects a clear lag around 550 days, which, however, contains only 5% of the original CCCD distribution (this is in contrast to the C IV lag for CT975, with a 1% peak observed in the reliable region of the CCCD, which JAVELIN recovers successfully). At the same time, JAVELIN finds a well-behaved peak at around 1000 days for the Si IV line in CT953, while the ICCF only finds a very shallow peak.

Since our main aim is to find statistically sound lags for our sample of luminous quasars, for the analysis and discussion in the next sections we will use the more conservative ICCF- and CCCD-based lags and error estimates as representative line lags for our sources.

5. Radius–Luminosity Relations

The radius–luminosity relation represents a milestone for the determination of the masses of BHs hosted by AGNs. Here we will update the radius–luminosity relation for the C IV emission line first presented by Peterson et al. (2005, 2006) and later extended to higher luminosities by Kaspi et al. (2007) and Trevese et al. (2014). To our knowledge, no determination of the radius–luminosity relations for the Ly α has previously been attempted, as no results for objects above $\lambda L_{\lambda}(1350 \text{ \AA}) = 10^{45} \text{ erg s}^{-1}$ had been reported until now.

In what follows we only construct radius–luminosity relations for objects where the lags are inconsistent with zero at a 1σ level, that is, when $\tau_{\text{cent}}/\sigma_{-} > 1$. UV $\lambda L_{\lambda}(1350 \text{ \AA})$ luminosities were obtained from the mean spectra of each quasar and are reported in Table 1. The errors represent the rms variation observed in the R-band continuum light curves. Scatter in the radius–luminosity correlations is given in each plot, where the first value corresponds to the observed scatter and the second value corresponds to the scatter due to measurement errors.

A linear regression was determined for each radius–luminosity relation using the bivariate method (BCES) of Akritas & Bershady (1996), which takes into account errors in both the lags and the luminosities. As our lag error determinations are not symmetrical, we use the mean of both confidence limits as a first guess for the lag error of each data point and iterate so that the final error bar considered (σ_{-} or σ_{+}) is determined by whether the points are

found above or below the best-fit solution. Convergence was always found after a few iterations.

5.1. The C IV Radius–Luminosity Relation

For luminosities below $\lambda L_{\lambda}(1350 \text{ \AA}) = 10^{45} \text{ erg s}^{-1}$, C IV lag measurements are compiled in Peterson et al. (2005, 2006) and Metzroth et al. (2006), and a very recent determination for NGC 5548 is found in De Rosa et al. (2015). Two sources above this luminosity limit have been published: S5 0836+71 by Kaspi et al. (2007), and PG 1247+267 by Trevese et al. (2014). Using the ICCF method, it is not possible, however, to determine the lag for PG 1247+267, as Trevese et al. (2014) also pointed out, and therefore we will not include this source in our C IV radius–luminosity determination. Our work adds to the list seven new high-luminosity sources, namely, CT1061, CT286, CT564, CT650, CT953, J214355, and J221516.

In Figure 7 we present the results from the linear regression to the C IV radius–luminosity relation, together with the lag and luminosity measurements. Following Kaspi et al. (2007), we write the C IV radius–luminosity in the following way:

$$\frac{R_{\text{C IV}}}{10 \text{ lt-days}} = (0.22 \pm 0.10) \left[\frac{\lambda L_{\lambda}(1345 \text{ \AA})}{10^{43} \text{ erg s}^{-1}} \right]^{(0.46 \pm 0.08)} \quad (1)$$

The updated C IV radius–luminosity relation is very close to that reported by Kaspi et al. (2007), albeit with slightly larger uncertainties. This is because we have included the mean from two lag measurements of NGC 4151 taken from Metzroth et al. (2006), which helped to bridge the luminosity gap between the more luminous Seyfert galaxies and the dwarf Seyfert NGC 4395 ($\lambda L_{\lambda}(1350 \text{ \AA}) \sim 10^{40} \text{ erg s}^{-1}$), but added more dispersion to the relation. Also, the two measurements for the NGC 4395 lag have been averaged, reducing the weight of the measurements at the very low luminosity end.

We remind the reader that a well-determined radius–luminosity relation for C IV does not solve the issues of using C IV as a well-calibrated mass estimator for AGNs, as the main problem with this line is the difficulty in determining a velocity that would reflect a virialized component of the velocity field of the line (see further discussion in Section 6.3 and, e.g., Baskin & Laor 2005; Denney 2012; Denney et al. 2016; Mejía-Restrepo et al. 2016, and references therein).

5.2. The Ly α Radius–Luminosity Relation

From our sample, CT1061, CT286, CT564, CT650, CT953, J214355, and J221516 show significant lags and well-determined uncertainties and will be considered for the determination of the Ly α radius–luminosity relation.

In order to have homogeneous measurements, we redetermined the Ly α lags for the Seyfert galaxies monitored by the International AGN Watch⁶ using the ICCF FR/RSS code that we employed with our sources. This is motivated by the improvements introduced to the FR/RSS code following Peterson et al. (2004), since all AGN Watch results were obtained previous to that date. We found significant lag constraints for NGC 3783 ($3.5_{-2.0}^{+1.6}$ days), NGC 7469 ($2.0_{-1.3}^{+0.2}$ days), Fairall 9 ($9.4_{-4.9}^{+5.1}$ days), and 3C 390.3 (61_{-42}^{+33} days), which were originally published by Reichert et al. (1994), Wanders et al. (1997), Rodríguez-Pascual et al. (1997), and O’Brien et al. (1998), respectively. Finally, we added the recent results for NGC 5548 from De Rosa et al. (2015),

⁶ <http://www.astronomy.ohio-state.edu/~agnwatch/>

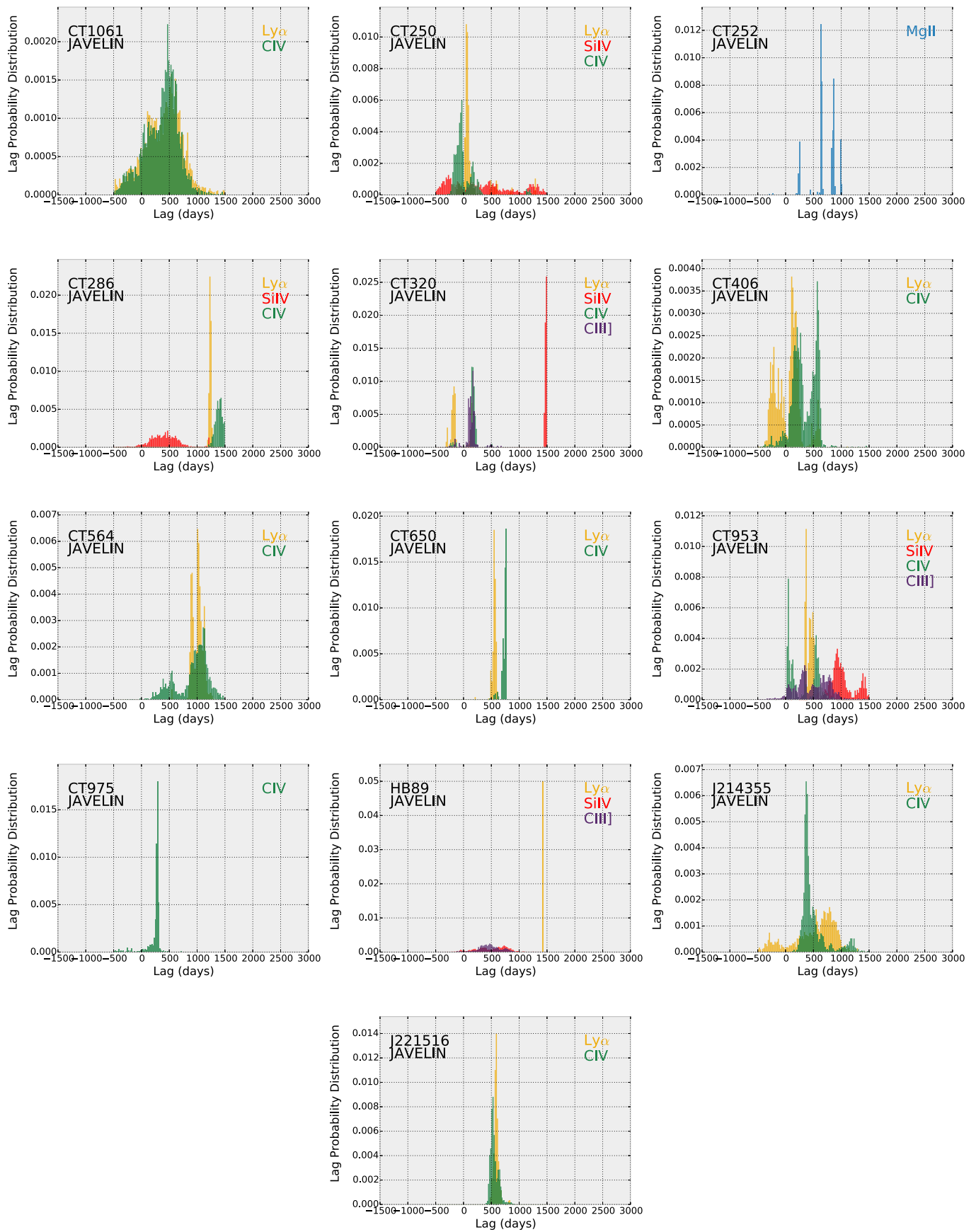


Figure 6. Lag probability distributions from the JAVELIN analysis.

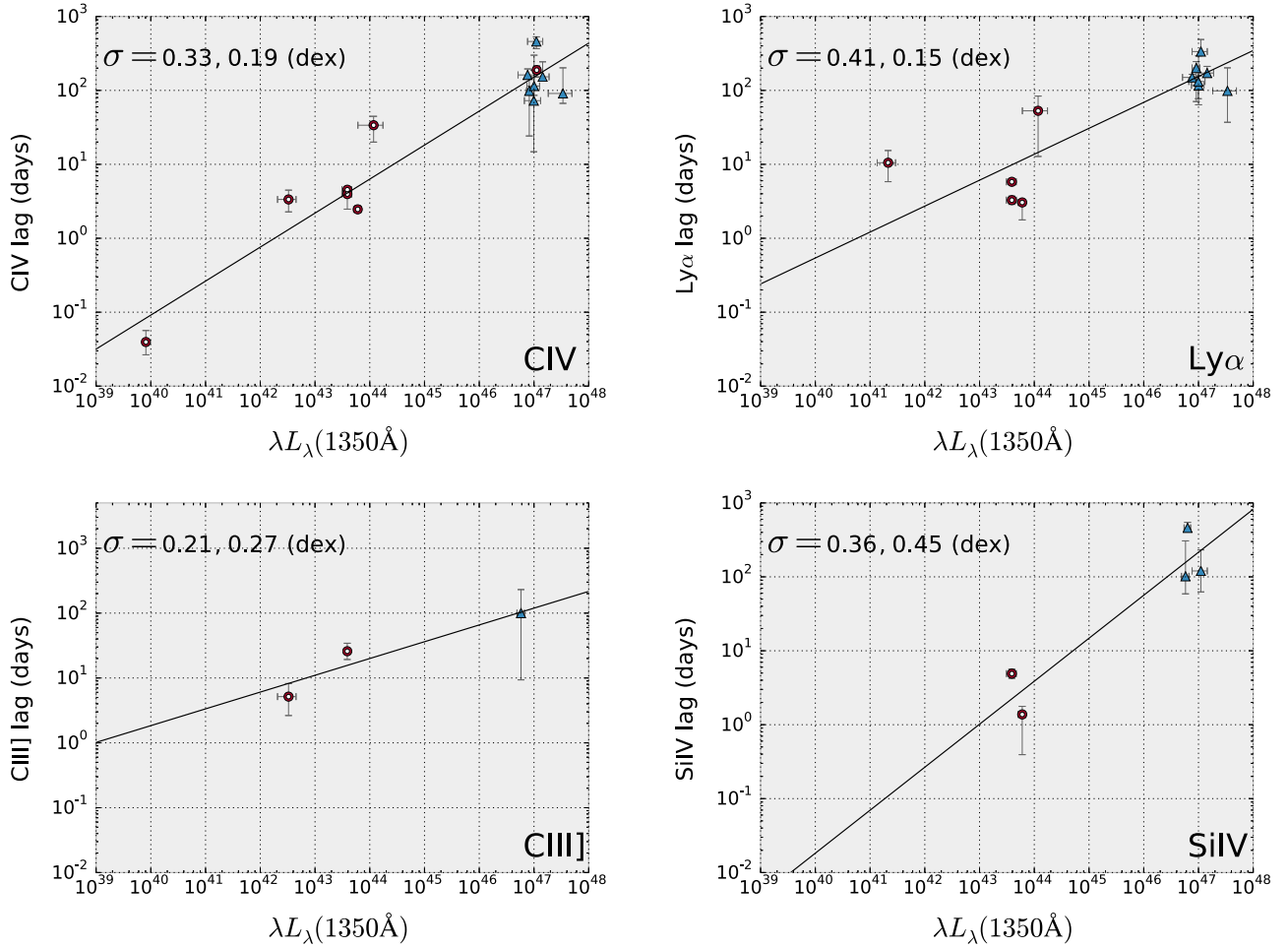


Figure 7. Radius–luminosity relations for the Ly α , C IV, C III], and Si IV emission lines. Our sources are presented with blue filled triangles, while sources taken from the literature are presented with red circles. The solid black lines show the linear regression to the data using a bivariate analysis. Two values of σ are shown at the top left of each panel, where the first value corresponds to the observed scatter and the second value corresponds to the scatter due to measurement errors.

which gives a lag of $5.9_{-0.3}^{+0.3}$ days during the “non-anomalous” period of the campaign.

The analytical expression found for the radius–luminosity relation using the linear regression is as follows:

$$\frac{R_{Ly\alpha}}{10 \text{ lt-days}} = (0.61 \pm 0.80) \left[\frac{\lambda L_{\lambda}(1345 \text{ \AA})}{10^{43} \text{ erg s}^{-1}} \right]^{(0.35 \pm 0.19)}. \quad (2)$$

Unfortunately, the Ly α radius–luminosity relation is not well constrained at the mid- and low-luminosity ends, as the International AGN Watch sources show a very large dispersion and no very low luminosity AGN has been monitored for this line.

5.3. The C III] and Si IV Radius–Luminosity Relations

A C III] radius–luminosity relation was determined using lag measurements for NGC 4151 (Metzroth et al. 2006) and a new analysis of the NGC 5548 light curves originally presented by Clavel et al. (1991), which gave a lag of $26.3_{-7.0}^{+8.3}$ days. This work adds HB89 as the only quasar from our sample that meets the requirement $\tau_{\text{cent}}/\sigma_{-} > 1$.

To determine an Si IV radius–luminosity relation, we reanalyzed the historical data for NGC 7496 and 3C 390.3 (Wanders et al. 1997 and O’Brien et al. 1998, respectively) but could only determine a significant lag of $1.4_{-1.1}^{+0.4}$ days for

NGC 7496. We add the recent determination for NGC 5548 from De Rosa et al. (2015). CT286, CT320, and HB89 lag measurements from our sample are included. These relationships are presented in Figure 7. The resulting analytical expressions are as follows:

$$\frac{R_{C \text{ III]}}}{10 \text{ lt-days}} = (1.10 \pm 0.77) \left[\frac{\lambda L_{\lambda}(1350 \text{ \AA})}{10^{43} \text{ erg s}^{-1}} \right]^{(0.26 \pm 0.16)}, \quad (3)$$

$$\frac{R_{Si \text{ IV}}}{10 \text{ lt-days}} = (0.10 \pm 0.10) \left[\frac{\lambda L_{\lambda}(1350 \text{ \AA})}{10^{43} \text{ erg s}^{-1}} \right]^{(0.58 \pm 0.16)}. \quad (4)$$

As with Ly α , the zero point of the Si IV radius–luminosity relation is very ambiguous because of the large dispersion observed in the Seyfert regime and the lack of any measurement for very low luminosity sources.

6. Discussion

6.1. Sources with Unexpected Line Variability

We have seen that 3/17 of our sources, i.e., $18_{-9}^{+14}\%$ assuming Poisson statistics (Gehrels 1986), show unexpected line variability, where the Ly α or Si IV emission-line light curves do not seem to follow that of the observed UV continuum.

One possibility is that in these objects these emission lines never responds to the observed continuum. Another possibility

is that this is a transitional behavior due to changes in the BLR properties or the ionizing source.

Disengagement of the line response has not been generally reported among the Seyfert galaxies that have been subject to RM campaigns, although a nonlinear response of C IV to the continuum variations was recognized in early observations of NGC 5548 (see Maoz 1994). In fact, a clearer “anomalous” behavior was seen in the very recent monitoring of NGC 5548, where a departure of the line emission light curves is observed during $\sim 1/3$ of the ~ 170 -day long campaign and where high-ionization emission lines, in particular C IV, show a stronger disagreement with the continuum light curve than low-ionization emission lines (Goad et al. 2016).

It seems that this behavior is more common in our sample of high-luminosity quasars, even though the number of variability “events” observed in the quasar light curves is usually smaller than those typically observed during seasonal monitoring campaigns of Seyfert galaxies. However, this result is based on limited data, while the different monitoring cadence, lengths of the campaigns, and wide ranges in BH masses and accretion rates (which might ultimately drive the variability of the sources) complicate the comparison beyond the scope of this paper.

It is interesting to notice, however, that while in NGC 5548 this behavior is strongest in the C IV line (with an ionization potential of 47.9 eV), in CT320, CT803, and J224743 it is Si IV and Ly α that behave in an anomalous way. This might suggest that the cause is a different ionization continuum, as predicted for accretion disks around BHs of different masses but similar accretion rates (e.g., Davis & Laor 2011), or seen in the relation between the α_{ox} index (indicative of the fractional output in the X-ray and optical bands) and AGN luminosity (e.g., Vignali et al. 2003).

6.2. Location of the Line-emitting Regions

One of the most significant and early results from RM in nearby Seyferts was the discovery that the BLR has a non-negligible radius and that different lines form at different distances from the central BH. From our cross-correlation analysis we can revisit this result and try to extend it to a wider luminosity range.

Figure 8 presents the ratio of Ly α , Si IV, C III], and C IV lags to H β lags for Seyfert galaxies monitored by the International AGN Watch and quasars from this work deemed reliable in Table 4. H β lags were determined using the $\lambda L_{\lambda}(5100 \text{ \AA})$ versus H β radius–luminosity correlation for the Clean2 sample in Bentz et al. (2013). Ly α , Si IV, C III], and C IV lags and associated confidence limits were taken from Table 4. Errors for these lines were assumed as the average of the lower and upper 1σ limits. Errors in the H β lags were taken as the scatter reported for the radius–luminosity correlation determined by Bentz et al. (2013), i.e., $\sigma^2 = 0.018$. The 5100 Å fluxes for our objects were obtained in the same way as in Section 2.1.2.

In general, we find a range of ratios that span up to a factor of 6. However, most line lags are consistent with their emitting regions being interior to the predicted location of H β . There is also no clear stratification among the four lines for which we have determined lags in this work, suggesting that they are all produced at similar distances from the central BH. There is no evidence for a clear dependency of the ratios with luminosity. This can be quantified comparing the lag cumulative distributions of Seyfert and quasars for *all* line ratios shown in Figure 8 using a K-S test, which yields a p -value of 0.23, suggesting that

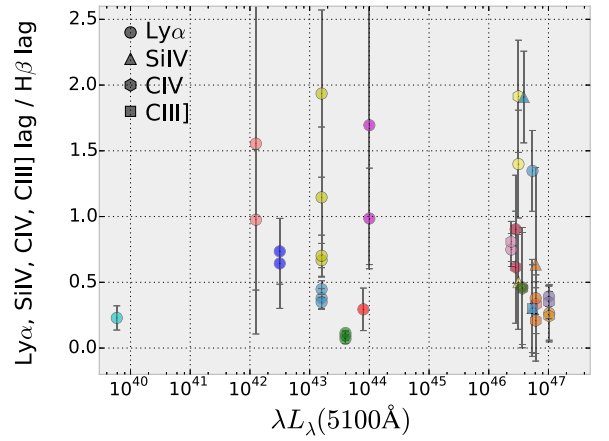


Figure 8. Ratio of Ly α , Si IV, C IV, and C III] to H β lags. The Ly α , Si IV, C IV, and C III] lags are those presented in Table 4, while the H β lags were predicted using the $\lambda L_{\lambda}(5100 \text{ \AA})$ vs. H β radius–luminosity correlation found in Bentz et al. (2013) and the inferred 5100 Å luminosities (see text). Different shapes correspond to different emission lines (see legend), while different colors correspond to different sources. Seyfert galaxies are NGC 3783, NGC 4151, NGC 5548, NGC 7469, and 3C 390.3, as stated before. We have also added data from the 1989 campaign of NGC 5548 and published by Clavel et al. (1991), as it includes the C III] emission line (after recalculating the lags using the ICCF FR/RSS code that we employed with our sources). The objects reported in this work are clustered at the high-luminosity end of the diagram. Errors in the Ly α , Si IV, C IV, and C III] lines were assumed as the average of the lower and upper 1σ confidence limits in the lag measurements, while the scatter in the H β radius–luminosity correlation for the Clean2 sample from Bentz et al. (2013) was taken as the H β lag errors.

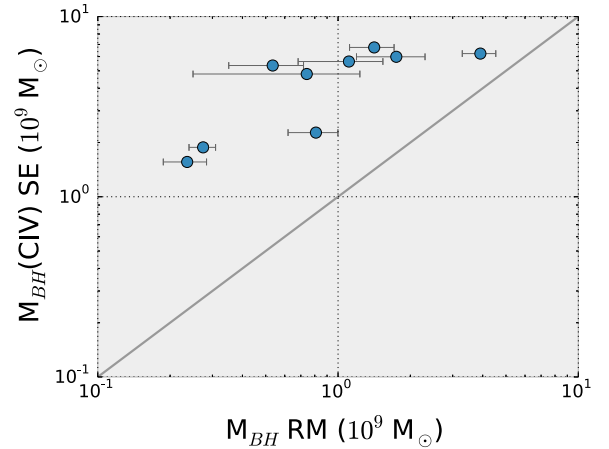


Figure 9. Comparison between SE- and RM-based BH masses, as presented in Tables 1 and 4. The thick gray line corresponds to the 1:1 relation.

the two distributions are very similar. This indicates that sources spanning 5 orders of magnitude in luminosity present a homologous BLR structure.

Notice the change in line ratios of the modern results for NGC 5548 (in blue) taken from De Rosa et al. (2015), when compared with the historic values (in yellow) published by Clavel et al. (1991). This seems to be evidence of a restructuring of the BLR in this source, with the line-emitting regions moving further in, despite a very small change in the UV and optical luminosities between these epochs. This also includes the H β location, as shown in Pei et al. (2017), with the lag about five times shorter than expected based on past measurements and the H β radius–luminosity correlation from Bentz et al. (2013).

Another interesting result is that all radius–luminosity relation slopes in Equations (1)–(4) are consistent at the 2σ level with the naïvely expected value of 0.5, as predicted by the assumption of a photoionized BLR where the mean ionization parameter and mean density at the peak emissivity for a certain line remain constant (see Bentz et al. 2013, for further discussion). Notice, however, that some of the slopes, such as that of the C III] line, have rather large errors.

6.3. BH Masses from RM and SE Methods

In Table 4 we give BH masses for sources with lags determined at a 1σ level in the uncertainties at both sides of the probability CCCD distribution, that is, $\tau_{\text{cent}}/\sigma_- > 1$ and $\tau_{\text{cent}}/\sigma_+ > 1$. Masses were obtained as $M_{\text{BH}}^{\text{RM}} = f \times \tau_{\text{cent}} \times c \times \text{FWHM}^2$, where f is the virial factor, τ_{cent} is the ICCF lag centroid reported in Table 4, and the FWHMs were measured from the mean spectra of each quasar and found in Table 2. Because of the noisy nature of the emission lines in the rms spectra of our objects (see Figure 3), we only measured the FWHMs from the total mean flux spectra. We have adopted a virial factor $f=1$, also assumed for the SE determinations. A good agreement is seen for RM masses obtained using different lines, with all results consistent within a 2σ level.

Inspection of Tables 1 and 4 shows that RM masses ($M_{\text{BH}}^{\text{RM}}$) are systematically smaller than those obtained using the C IV SE method ($M_{\text{BH}}^{\text{SE}}$), which were determined using $M_{\text{BH}}^{\text{SE}} = 10^{6.353} \times (L_{1450})^{0.599} \times \text{FWHM}^2$ as presented in Mejía-Restrepo et al. (2016). Again, the FWHM values are those presented in Table 1. The results can be seen in Figure 9, where the mean of the RM masses is plotted when lags from more than one line are available for a single object. Our results suggest that, on average, $M_{\text{BH}}^{\text{SE}}$ are overestimated when compared with $M_{\text{BH}}^{\text{RM}}$. The discrepancy is probably driven by the nonvirial behavior of the C IV line width. The SE cross-calibration of C IV assumes that the region responsible for the emission of this line obeys $R_{\text{H}\beta}/R_{\text{C IV}} = (\text{FWHM}(\text{H}\beta)/\text{FWHM}(\text{C IV}))^{-2}$ (since SE masses obtained from H β and C IV must satisfy $M_{\text{BH}}^{\text{SE}}(\text{H}\beta) = M_{\text{BH}}^{\text{SE}}(\text{C IV})$). As we just determined for our quasars, $R_{\text{C IV}}/R_{\text{H}\beta} \sim 0.5$, and we would expect that $(\text{FWHM}(\text{H}\beta)/\text{FWHM}(\text{C IV}))^2 \sim 0.5$ or $\text{FWHM}(\text{C IV}) \sim 1.4 \times \text{FWHM}(\text{H}\beta)$ for a virialized system. However, typically it is found that C IV is narrower than this, suggesting a dominant nonvirialized component in many sources (see Trakhtenbrot & Netzer 2012).

7. Summary

For the first time we have presented RM results for a substantial number of luminous quasars found at $z \gtrsim 2$. From our results we can summarize the following:

1. Out of 17 quasars with spectroscopic follow-up, 14 show that all their emission-line light curves seem to reverberate in response to the variations observed in the continuum light curves, while 3/17 show peculiar behavior in one emission line. This might suggest that the observed R -band continuum in these three sources does not follow the changes that the ionizing continuum experiences.
2. Reliable lag measurements are determined for 11 quasars for the Ly α emission line, 5 for the Si IV emission line, 11 for the C IV emission line, and 2 for the C III] emission line (Table 4). However, only $\sim 1/2$ of the determined lags have $\tau_{\text{cent}}/\sigma > 1$ and are therefore sufficiently constrained to allow for the determination of BH masses.
3. Radius–luminosity relations for Ly α , Si IV, C IV, and C III] are presented using our data and previous lag determinations. Slopes are well constrained for all correlations and are found to be less than 2σ away from the predicted value of 0.5, although the Ly α and C III] relations present large fractional errors.
4. We find that the regions responsible for the emission of Ly α , Si IV, C IV, and C III] are commonly interior to that producing H β . At the same time, there is no clear stratification among them. This is found to be the case across 5 orders of magnitude in continuum luminosity.
5. For those quasars with lags determined at a 1σ level (for both σ_- and σ_+), we determined BH masses using the observed emission-line FWHMs. The RM masses are systematically smaller than those determined from SE C IV calibrations. This is consistent with a significant nonvirialized component to the C IV line profile.

This project would had never been possible without the support of the Chilean National TAC (CNTAC), which for more than 10 yr allocated hundreds of nights of telescope time to conduct our reverberation campaign. We also thank Brad Peterson and Mario Hamuy for facilitating code used in the analysis of the data. Finally, we also thank the anonymous referee for the suggestion to use MC to determine line light-curve errors. P.L. acknowledges support by Fondecyt over all these years, and in particular from project No. 1161184.

Appendix

Table 5 presents the emission-line and R -band continuum light curves for the quasar CT1061. The remaining light curves can be downloaded from the electronic journal database. In all tables dates are expressed in JD $-2,450,000$ days and fluxes in units of $10^{-14} \text{ erg s}^{-1} \text{ cm}^{-2}$ for the line measurements and $10^{-16} \text{ erg s}^{-1} \text{ cm}^{-2} \text{ \AA}^{-1}$ for the R -band light curves.

Table 5
Emission Line and Continuum Quasar Light Curves

Ly α			Si IV			C IV			C III]			R		
JD	Flux	Error	JD	Flux	Error	JD	Flux	Error	JD	Flux	Error	JD	Flux	Error
5270.8	27.19	0.44	5270.8	2.06	0.26	5270.8	8.12	0.12	5270.8	4.15	0.35	3403.9	5.50	0.08
5280.7	27.39	0.53	5280.7	1.90	0.32	5280.7	8.19	0.16	5280.7	3.96	0.31	3444.8	5.48	0.08
5658.6	27.04	0.46	5658.6	2.06	0.24	5658.6	8.01	0.13	5658.6	3.99	0.24	3490.7	5.55	0.08
5917.8	27.28	0.53	5917.8	2.04	0.26	5917.8	8.03	0.17	5917.8	4.20	0.29	3781.7	5.70	0.08
5945.8	27.26	0.50	5945.8	2.12	0.22	5945.8	8.12	0.14	5945.8	4.00	0.28	3846.7	5.52	0.08
6015.7	26.72	0.54	6015.7	1.92	0.26	6015.7	7.86	0.19	6015.7	3.73	0.30	3894.5	5.58	0.08
6017.7	27.42	0.50	6017.7	2.10	0.29	6017.7	8.10	0.17	6017.7	3.73	0.44	4140.9	5.48	0.08

Table 5
(Continued)

Ly α			Si IV			C IV			C III]			R		
JD	Flux	Error	JD	Flux	Error	JD	Flux	Error	JD	Flux	Error	JD	Flux	Error
6048.6	26.95	0.45	6048.6	1.95	0.29	6048.6	7.96	0.13	6048.6	4.36	0.33	4154.8	5.53	0.08
6298.8	26.83	0.37	6298.8	2.00	0.22	6298.8	8.04	0.12	6298.8	4.00	0.26	4168.9	5.58	0.08
6723.8	26.65	0.36	6723.8	1.90	0.20	6723.8	7.84	0.08	6723.8	4.46	0.31	4258.6	5.63	0.08
6783.6	26.68	0.53	6783.6	1.92	0.24	6783.6	8.00	0.21	6783.6	4.12	0.30	4272.5	5.69	0.08
7020.8	26.20	0.40	7020.8	1.90	0.24	7020.8	7.46	0.25	7020.8	3.77	0.34	4505.8	6.21	0.09
7759.0	26.30	0.47	7759.0	1.96	0.27	7759.0	7.75	0.11	7759.0	3.75	0.24	4579.7	6.36	0.09
...	4580.5	6.22	0.09
...	4856.7	6.58	0.09
...	4889.8	6.71	0.09
...	4910.8	6.63	0.09
...	4944.7	6.76	0.09
...	5010.5	6.78	0.09
...	5235.8	6.48	0.09
...	5264.7	6.50	0.09
...	5270.8	6.70	0.04
...	5274.7	6.60	0.09
...	5280.7	6.65	0.04
...	5306.7	6.55	0.09
...	5628.8	6.16	0.08
...	5628.8	6.20	0.09
...	5653.8	6.21	0.09
...	5653.8	6.25	0.09
...	5658.6	6.21	0.04
...	5666.7	6.32	0.09
...	5666.7	6.25	0.09
...	5738.5	6.12	0.08
...	5738.5	6.13	0.08
...	5917.8	6.01	0.04
...	5929.7	6.01	0.08
...	5929.7	5.96	0.08
...	5945.8	5.95	0.04
...	6013.6	5.79	0.08
...	6013.6	5.76	0.08
...	6015.7	5.54	0.04
...	6017.7	5.86	0.04
...	6033.6	5.79	0.08
...	6033.6	5.75	0.08
...	6048.6	5.85	0.04
...	6049.5	5.72	0.08
...	6049.5	5.70	0.08
...	6298.7	5.53	0.08
...	6298.7	5.44	0.08
...	6298.8	5.54	0.04
...	6303.7	5.54	0.08
...	6303.8	5.63	0.11
...	6306.7	5.60	0.08
...	6306.7	5.50	0.08
...	6400.6	5.33	0.07
...	6723.8	5.19	0.04
...	6783.6	5.14	0.04
...	7020.8	5.26	0.04
...	7109.6	5.28	0.07
...	7123.6	5.24	0.07
...	7152.5	5.40	0.07
...	7181.5	5.37	0.07
...	7182.4	5.38	0.07
...	7225.5	5.35	0.29
...	7759.0	5.34	0.04

Note. Light curves for all quasars are available in the online journal. The emission-line and *R*-band continuum light curves for CT1061 are shown here for guidance regarding its form and content.

(This table is available in its entirety in machine-readable form.)

ORCID iDs

Hagai Netzer  <https://orcid.org/0000-0002-6766-0260>
 Nidia Morrell  <https://orcid.org/0000-0003-2535-3091>
 Julián Mejía-Restrepo  <https://orcid.org/0000-0001-8450-7463>
 Paula Sánchez-Sáez  <https://orcid.org/0000-0003-0820-4692>
 Jorge Martínez-Palomera  <https://orcid.org/0000-0002-7395-4935>

References

- Akritas, M. G., & Bershad, M. A. 1996, *ApJ*, 470, 706
 Alexander, T. 1997, *ASSL*, 218, 163
 Baskin, A., & Laor, A. 2005, *MNRAS*, 356, 1029
 Bentz, M. C., Denney, K. D., Grier, C. J., et al. 2013, *ApJ*, 767, 149
 Bentz, M. C., Peterson, B. M., Netzer, H., Pogge, R. W., & Vestergaard, M. 2009, *ApJ*, 697, 160
 Bentz, M. C., Peterson, B. M., Pogge, R. W., Vestergaard, M., & Onken, C. A. 2006, *ApJ*, 644, 133
 Blandford, R. D., & McKee, C. F. 1982, *ApJ*, 255, 419
 Bongiorno, A., Zamorani, G., Gavignaud, I., et al. 2007, *A&A*, 472, 443
 Cardelli, J. A., Clayton, G. C., & Mathis, J. S. 1989, *ApJ*, 345, 245
 Chhetri, R., Ekers, R. D., Jones, P. A., & Ricci, R. 2013, *MNRAS*, 434, 956
 Cirasuolo, M., Magliocchetti, M., Celotti, A., & Danese, L. 2003, *MNRAS*, 341, 993
 Clavel, J., Reichert, G. A., Alloin, D., et al. 1991, *ApJ*, 366, 64
 Condon, J. J., Cotton, W. D., Greisen, E. W., et al. 1998, *AJ*, 115, 1693
 Croom, S. M., Smith, R. J., Boyle, B. J., et al. 2004, *MNRAS*, 349, 1397
 Cutri, R. M., Skrutskie, M. F., van Dyk, S., et al. 2003, *yCat*, 2246
 Davis, S. W., & Laor, A. 2011, *ApJ*, 728, 98
 De Rosa, G., Peterson, B. M., Ely, J., et al. 2015, *ApJ*, 806, 128
 Denney, K. D. 2012, *ApJ*, 759, 44
 Denney, K. D., Horne, K., Shen, Y., et al. 2016, *ApJS*, 224, 14
 Edelson, R., Gelbord, J. M., Horne, K., et al. 2015, *ApJ*, 806, 129
 Edelson, R. A., & Krolik, J. H. 1988, *ApJ*, 333, 646
 Fausnaugh, M. M., Denney, K. D., Barth, A. J., et al. 2016, *ApJ*, 821, 56
 Gehrels, N. 1986, *ApJ*, 303, 336
 Goad, M. R., Korista, K. T., De Rosa, G., et al. 2016, *ApJ*, 824, 11
 Grier, C. J., Pancoast, A., Barth, A. J., et al. 2017, *ApJ*, 849, 146
 Hewitt, A., & Burbidge, G. 1989, *ApJS*, 69, 1
 Kasliwal, V. P., Vogeley, M. S., & Richards, G. T. 2015, *MNRAS*, 451, 4328
 Kaspi, S., Brandt, W. N., Maoz, D., et al. 2007, *ApJ*, 659, 997
 Kaspi, S., Maoz, D., Netzer, H., et al. 2005, *ApJ*, 629, 61
 Kaspi, S., Smith, P. S., Netzer, H., et al. 2000, *ApJ*, 533, 631
 Kelly, B. C., Bechtold, J., & Siemiginowska, A. 2009, *ApJ*, 698, 895
 Kormendy, J., & Ho, L. C. 2013, *ARA&A*, 51, 511
 Maoz, D. 1994, in ASP Conf. Ser. 69, Reverberation Mapping of the Broad-Line Region in Active Galactic Nuclei, ed. P. M. Gondhalekar, K. Horne, & B. M. Peterson (San Francisco, CA: ASP), 95
 Maoz, D., Netzer, H., Leibowitz, E., et al. 1990, *ApJ*, 351, 75
 Mauch, T., Murphy, T., Buttery, H. J., et al. 2003, *MNRAS*, 342, 1117
 Maza, J., Ruiz, M. T., Gonzalez, L. E., Wischnjewsky, M., & Antezana, R. 1993, *RMxAA*, 25, 51
 Maza, J., Wischnjewsky, M., & Antezana, R. 1996, *RMxAA*, 32, 35
 Mejía-Restrepo, J. E., Trakhtenbrot, B., Lira, P., Netzer, H., & Capellupo, D. M. 2016, *MNRAS*, 460, 187
 Metzroth, K. G., Onken, C. A., & Peterson, B. M. 2006, *ApJ*, 647, 901
 Momjian, E., Carilli, C. L., Walter, F., & Venemans, B. 2014, *AJ*, 147, 6
 O'Brien, P. T., Dietrich, M., Leighly, K., et al. 1998, *ApJ*, 509, 163
 Onken, C. A., & Peterson, B. M. 2002, *ApJ*, 572, 746
 Pei, L., Fausnaugh, M. M., Barth, A. J., et al. 2017, *ApJ*, 837, 131
 Peterson, B. M., Bentz, M. C., Desroches, L.-B., et al. 2005, *ApJ*, 632, 799
 Peterson, B. M., Bentz, M. C., Desroches, L.-B., et al. 2006, *ApJ*, 641, 638
 Peterson, B. M., Ferrarese, L., Gilbert, K. M., et al. 2004, *ApJ*, 613, 682
 Peterson, B. M., Wanders, I., Horne, K., et al. 1998, *PASP*, 110, 660
 Reichert, G. A., Rodríguez-Pascual, P. M., Alloin, D., et al. 1994, *ApJ*, 425, 582
 Rodríguez-Pascual, P. M., Alloin, D., Clavel, J., et al. 1997, *ApJS*, 110, 9
 Ross, N. P., McGreer, I. D., White, M., et al. 2013, *ApJ*, 773, 14
 Saturni, F. G., Trevese, D., Vagnetti, F., Perna, M., & Dadina, M. 2016, *A&A*, 587, A43
 Shemmer, O., Netzer, H., Maiolino, R., et al. 2004, *ApJ*, 614, 547
 Trakhtenbrot, B., & Netzer, H. 2012, *MNRAS*, 427, 3081
 Trevese, D., Perna, M., Vagnetti, F., Saturni, F. G., & Dadina, M. 2014, *ApJ*, 795, 164
 Trevese, D., Stirpe, G., Vagnetti, F., Zitelli, V., & Paris, D. 2006, in ASP Conf. Ser. 360, AGN Variability from X-Rays to Radio Waves, ed. C. M. Gaskell et al. (San Francisco, CA: ASP), 201
 Ulrich, M.-H., Courvoisier, T. J.-L., & Wamsteker, W. 1993, *ApJ*, 411, 125
 Vanden Berk, D. E., Richards, G. T., Bauer, A., et al. 2001, *AJ*, 122, 549
 Vignali, C., Brandt, W. N., & Schneider, D. P. 2003, *AJ*, 125, 433
 Wanders, I., Peterson, B. M., Alloin, D., et al. 1997, *ApJS*, 113, 69
 Wang, R., Carilli, C. L., Beelen, A., et al. 2007, *AJ*, 134, 617
 Welsh, W., Robinson, E. L., Hill, G., et al. 2000, *BAAS*, 32, 39.13
 Zu, Y., Kochanek, C. S., Kozłowski, S., & Udalski, A. 2013, *ApJ*, 765, 106
 Zu, Y., Kochanek, C. S., & Peterson, B. M. 2011, *ApJ*, 735, 80